IMPROVING LAND COVER CLASSIFICATION USING TEXTURE PATTERNS DERIVED FROM MICRO-SCALE DIGITAL ELEVATION MODELS

by

John D. Klier B.S., M.S.

A dissertation submitted to the Graduate Council of
Texas State University in partial fulfillment
of the requirements for the degree of
Doctor of Philosophy
with a Major in Geography-GIScience
May 2022

Committee Members

Nathan Currit, Chair

Jennifer Jensen

Richard Earl

Justin Williams

FAIR USE AND AUTHOR'S PERMISSION STATEMENT

Fair Use

Duplication Permission

DEDICATION

To my mom and dad for always pushing me to do better. Especially to my mom who passed away just prior to finishing this work. Also, to my wife and two daughters for always being supportive in my dedication to finishing this degree.

ACKNOWLEGEMENTS

I want to express my sincere appreciation to all my committee members. Dr. Nate Currit, it has been a long haul, thank you for sticking with me. Dr. Jennifer Jensen, I really enjoyed all of the adventures we had flying drones, even the one that caught fire. Dr. Richard Earl, I have great memories of the field methods classes, thank you for introducing me to Freeman Ranch. Dr. Justin Williams, thank you for your input and making my documents the best it could be.

TABLE OF CONTENTS

ACKNOWLEGEMENTS v

LIST OF TABLES viii

LIST OF FIGURES ix

ABSTRACT x

CHAPTERS

I. INTRODUCTION 1

II. LITERATURE REVIEW.....8

Land Cover Change Detection.....8

Image Texture for Land Cover Classification 14

Manual and Automated Photogrammetry.....19

Lidar.....21

Comparing lidar and Structure from Motion 24

Image Classification Algorithms and Techniques 25

III. DATA & METHODOLOGY 29

Study Area 29

Data Collection of Tree Canopy Elevation Textures.....35

UAS Image Collection.....35

Structure from Motion Processing.....42

Land-Cover Classifications and Comparisons.....44

GEOBIA and The Gray level Co-occurrence Matrix Classification 45

Pixel-based, Supervised Maximum Likelihood Classification 51

NDVI Analysis using NAIP Imagery 54

Accuracy Assessment 55

IV. RESULTS AND DISCUSSION 59

Overall, Producer's and User's Accuracies 59

Pair-wise Comparisons 64

Reconsidering Texture as an Ancillary Data Source 67

Canopy Structure 67

Scale Texture 68

Temporal Texture 70

V. CONCLUSION 73

Study Limitations 77

Future Work 78

APPENDIX 82

Aerial Photography Platforms 82

REFERENCES 88

LIST OF TABLES

Table		Page
1.	Texas Ecological System Classification Project ecosystems located in Freeman Ranch	32
2.	Sample of flight log data created by autopilot	40
3.	Error matrices for the three classification methods	61
4.	Classification significance levels	63
5.	Comparative classification analyses	65

LIST OF FIGURES

Figure **Page**

1. National Agriculture Imagery Program (NAIP) image showing a portion of the study area....13

2. National Elevation Dataset (NED) 1/9 arc second (3 meter) resolution DEM and NAIP imagery at 1-meter resolution of the same area....18

3. Polygon indicates location of study area located 11 kilometers Northwest of San Marcos....30

4. Ecosystems of Freeman Ranch....33

5. Study area within the Freeman Ranch Boundary....34

6. DEM (left) created from UAS imagery indicating approximately 7.5cm....37

7. Example of flight plan overlaid on aerial imagery....41

8. Data Processing Workflow....43

9. Results of the GEOBIA segmentation process using Trimble eCognition....48

10. Table showing RGB signatures of study area tree classes....52

11. Drone imagery classified using the maximum likelihood classifier....53

12. 3D Robotics X8 Rotorcraft Drone....84

13. Hawkeye AreoHawk Survey Grade Fixed Wing UAS....86

ABSTRACT

Historically the determination of land cover types has relied upon techniques that analyze reflected spectral energy in the visible or near infrared wavelengths. Often, these wavelength bands are used in combination to produce vegetation indices like the Normalized Difference Vegetation Index (NDVI).

Data derived from sources such as Light Detection and Ranging (LiDAR) or Structure from Motion (SfM) have been primarily utilized for construction of elevation models and contour maps. The resolution of this data generally allows for detailed reconstruction of the subject area terrain where one can see objects such as rivers, streams, buildings, stands of trees, etc.

In the past 10 years drone technology has become available to the general public and with it a researcher is able to gather high resolution data in a fixed flight path where the camera orientation for each photo in relation to the ground is known. This detail subsequently has allowed for the creation of elevation models that show detail in individual tree crowns. This dissertation uses drone technology to examine the role of tree canopy texture, derived from a hyperspatial digital elevation model, in identifying individual tree species. The research questions addressed in this dissertation include: (1) Are texture patterns derived from hyperspatial digital elevation models (DEM) of the tree canopy indicators of individual tree species? (2) What is the role of texture in determining species-level assemblages and/or individual tree entities? (3) Can texture alone match reflectance-based land-use/land-cover (LULC) detection methods in

accuracy of classification? To answer these questions three classification techniques are compared for a mixed canopy environment in the Texas, USA Hill Country: (1) object-based image analysis of drone-based canopy texture, (2) maximum likelihood classification of multispectral drone imagery, and (3) object-based image analysis of NDVI derived from National Agricultural Imagery Program aerial photography. Findings from this comparison suggest that an analysis of texture alone can match the results of multispectral image classification techniques. Findings lead to the conclusions that canopy texture is a key indicator of individual tree species and that hyperspatial DEMs adequately capture unique differences in tree species.

I. INTRODUCTION

Human population increases and resultant landscape alterations are leading causes of the global biodiversity crisis (Wilson 1988; Lambin et al. 2001; Groom, Meffe, and Carroll 2006). Historic and current literature on human induced land cover change identifies numerous and complex drivers of change, including social, economic and demographic conditions (Meyer and Turner 1992; Geist and Lambin 2002; Luus, Robinson, and Deadman 2013). A critical component of understanding the drivers of land cover change, which is inherent in all previous studies, is to have an accurate depiction of where, and at what pace, change is occurring. Therefore, expeditious and accurate land cover change detection methods are key to monitoring and modeling critical environmental challenges.

A primary means of monitoring land-cover change is via remote spectral measurements from airborne or satellite platforms. Such remote sensing systems provide consistent data at a regular interval appropriate for detecting seasonal, annual, and decadal shifts in land-cover patterns. Each sensor is designed to provide data at specific spectral, spatial, radiometric and temporal resolutions. Although Land Use/Land Cover (LULC) change detection methods and technologies have advanced over the past decades, they suffer from resolution limitations that typically don't capture fine spatial details of a complex ecosystem. Existing methods tend to observe landscape change at pixel resolutions amenable to detecting changes of large contiguous entities, such as a coniferous forest or riparian wetlands. At these scales, change is often well established by the time it is observable in the data. If the land cover change is detected early enough, steps can often be taken to minimize the impacts or possibly stop the damage altogether

before the change reaches the critical tipping point of irreversibility. These subtle changes can be easily detected using the drone-based sensing methods utilized in this study and others (Cunliffe, Brazier, and Anderson 2016).

To illustrate the scope and scale of land cover change I refer to a recent study in the western Unites States. Land cover change was analyzed between the years 1973 and 2000 in 30 distinct ecological regions within six main regional groupings which share similar physical and biological characteristics (Soulard and Sleeter 2012). The authors found that the average overall change for this period was 5.8% with a range from 0.5% (in the Chihuahuan Desert Ecoregion) to 28.0% (in the Puget Lowland Ecoregion).

The ecoregions showing the greatest change are the easiest to detect simply because their changes are easily discernible with coarse resolution (10-meter resolution or greater) sensors. However, there are also other diverse ecosystems indicating lower than average change. The Sierra Nevada Ecoregion at 5.0% and the Wasatch Mountains Ecoregion at 2.0% are two examples of regions with below average change. The Wasatch Mountains Ecoregion is indicated to cover 44,176 square kilometers. A 2.0% change to 44,176 square kilometers is 883.5 square kilometers, which when divided by the 27 years covered by the study, equals an average of 32 square kilometers of change per annum. Previous research has indicated that land cover change tends to start slowly and accelerate over time (Meyer and Turner 1992; Lambin et al. 2001). What kind of an impact 32 square kilometers of change per annum would have would vary from region to region and depend upon the spatial pattern of change. It may be concentrated in one place or it may be widely dispersed. If the 32 square kilometers of change were uniformly dispersed across the Wasatch Mountain Ecoregion the change would be undetectable by

many sensors because the within pixel variation of change is not known due to the relatively low resolution of the imagery.

Hyperspatial imagery (imagery of a very high spatial resolution) is being utilized more frequently in remote sensing studies. There is no current definition of what resolution is considered hyperspatial, but a search of recent literature finds that most authors utilizing what they call hyperspatial imagery use data ranging from 3 cm to 10 cm resolution (Black et al. 2014; Tamminga et al. 2015). In a paper studying limits on tree density, Greenberg, Dobrowski and Vanderbilt (2009) define hyperspatial as pixels smaller than tree crowns. Based upon the resolution ranges in these previous studies, hyperspatial in this study will refer to imagery with a spatial resolution of 10 cm or lower.

Publicly accessible satellite imagery does not currently include hyperspatial data. While sensors flown on aircraft have been capable of gathering hyperspatial data for quite some time they are often limited to no better than ½ meter resolution. There are many types of analysis that do not require hyperspatial data so the additional cost in equipment, time and storage are not included in a projects' budget. Until recently aircraft-derived hyperspatial photography came from specialized equipment meant to be mounted on the airframe. Today off the shelf hand-held cameras are very capable sensors for gathering hyperspatial data. They are typically limited to the RGB spectrum unless modified to allow sensing of the NIR bands.

Recent literature indicates there are many uses for hyperspatial data and increasing the accuracy of biodiversity maps is a very common theme in publications over the past ten years (Murphy et al. 2008; Culbert et al. 2012; Agarwal et al. 2013;

Tamminga et al. 2015). With hyperspatial imagery it becomes possible to identify individual biological entities. What used to be just a stand of trees now can be identified as individual trees of a particular species. (Franklin et al. 2000; Turner et al. 2003; Kerr and Ostrovsky 2003; Moskal and Franklin 2004; Boyd and Danson 2005; Liu, Hu, and Peng 2005; Murphy et al. 2008; Greenberg, Dobrowski, and Vanderbilt 2009; Strecha et al. 2012; Agarwal et al. 2013; Rocchini et al. 2013). Hyperspatial data is additionally important for monitoring individual plant species' health and disease occurrence (Moskal and Franklin 2004; Greenberg, Dobrowski, and Vanderbilt 2009).

While data gathered hyperspatially would seemingly be advantageous, there are some issues to be considered when attempting to use this data for land cover studies. When mapping urban tree species in India, Agarwal et al. (2013) found that diffferences in sunlit vs. non-sunlit leaves made detection of tree canopies challenging when using traditional pixel-based classification techniques. Their study showed the value in utilizing object-oriented classification to overcome these challenges that arise with hyperspatial imagery.

A tree characteristic critical for accurate species level identification that only becomes apparent when using hyperspatial imagery is canopy texture. Canopy texture derives from the arrangement of leaves and twigs in relationship to each other and to the sensor. With imagery of a fine enough resolution to resolve individual leaves on trees, canopy texture patterns can be identified. These texture patterns may be unique to individual tree species and thus can be used for automated species detection methods.

Data can be both hyperspectral and hyperspatial. In comparing data that are either hyperspectral or hyperspatial there are significant differences between what can be

derived from the data and the ease with which one can obtain that data. The availability of existing sensors is one of the biggest differences. Hyperspatial data can be gathered from off the shelf low cost cameras which can be easily fitted to a small unammned aircraft. Hyperspectral data requires a much more expensive sensor that until very recently could only be fitted to a manned aircraft or a satellite. There may be a need for data that is both hyperspatial and hyperspectral but that should not always be the case. A secondary benefit of this study will show that inexpensive hyperspatial imagery can be a source for certain types of land cover classification.

In this study I seek to demonstrate how hyperspatial mapping may provide adequate and prompt detection of ecosystem disturbances prior to significant shifts in ecosystem functioning. While a sensor with 30x30 meter resolution might detect large homogenous LULC changes, change may be well established before it is identified. This study seeks to establish a methodological framework for detecting change at a hyperspatial resolution that will allows for early detection of portending changes.

The focus of my research introduces a methodology for distinguishing the individual landscape components (i.e., individual trees and groups of trees of the same species rather than just “forest” and “non-forest”) and shows that the combination of texture (through object-based image analysis) and traditional land cover change detection methods is superior to traditional spectral methods alone because it incorporates a more complete set of inherent characteristics of the object being remotely sensed, namely texture. To accomplish this, texture and reflectance were used in combination to detect individual landscape objects rather than broad landscape classes.

With this focus I answered the following questions:

1. Are texture patterns derived from hyperspatial digital surface models (DSM) of the tree canopy indicators of individual tree species?
2. What is the role of texture in determining species-level assemblages and individual tree entities?
3. Can texture alone match reflectance-based LULC detection methods in accuracy of classification?

Question one addresses whether patterns of tree canopy texture derived from hyperspatial DSM's can be utilized for identifying tree species. Answering this question requires that (1) the DSM be of a resolution where elevations within the canopy can be resolved, and (2) the patterns derived from these elevations are significantly different between species so that the species can be detected and classified through object-based image analysis.

Question two builds on the findings of question one by seeking to establish a relationship between the physical construction of the canopy and the texture pattern collected from the DSM. To analyze these patterns and derive meaningful information from them, this study will utilize a statistical method called Gray Level Co-occurrence Matrix (GLCM). GLCM analyzes the gray level intensity between a pixel and its neighbors. Using the GLCM statistical method in this study will quantify the texture patterns of each species which will in turn allow to differentiate between those species. This quantification shows what part of the overall classification texture plays.

Question three directly addresses the question I believe would be of most interested: can this study provide a new method of classification that is at least as good as commonly used spectral data and classification techniques? To answer this question, the

texture analysis is compared to two other reflectance-based classification methods of the study area and significant differences are compared.

II. LITERATURE REVIEW

Land Cover Change Detection

Land cover is the biophysical covering of the Earth—the vegetation, geologic features or built-up environment that constitute the land surface. Land cover change refers to the change over time that occurs in the land cover and can be placed within two main categories: conversion from one land cover to another and modification within a land cover type (Meyer and Turner 1992). The causes of land cover change may be proximate (i.e., direct and localized causes of change) or underlying (i.e., indirect and often distant causes of change). Proximate causes generally refer to physical actions taken on the land-cover such as agricultural expansion or timber harvesting. Underlying causes constrain proximate causes and often arise at the intersection of complex political, demographic, technological, cultural, meteorological/climate and economic dimensions (Meyer and Turner 1992; Lambin et al. 2001; Geist and Lambin 2002). Underlying causes often originate at regional to global scales (Meyer and Turner 1992; Lambin, Geist, and Lepers 2003; Lambin and Geist 2006).

Amazonian deforestation is an example of proximate and underlying causes occurring in tandem. Geist and Lambin (2002) found that 96% of deforestation in Amazonia was due to agricultural expansion, and that the underlying drivers of expansion were economic, institutional, technological, cultural and demographic in nature. They cautioned against using single-factor explanations of deforestation yet noted that claims of irreducible complexity hinder progress toward meaningful solutions. Other studies indicate increased cropland is a regionally significant land cover change and that it has increased between 300 and 500% worldwide from the 1700s to the late 20th century

(Meyer and Turner 1992; Lambin et al. 2001). Meyer and Turner (1992) imply that at least some of the change is driven by perceived needs which would lead to land being of little benefit until the time when it is reutilized or re-forested.

In more industrialized nations where population growth is slowing and agriculture production has become increasingly efficient, the trend of change from forest to cropland has shifted. The largest increase in land cover change in these areas is change to urban and developed land cover types. Most often this change comes from former agricultural lands, which were often formerly forests or grasslands (Drummond and Auch 2016; Loveland and Acevedo 2016).

Land cover change has accelerated substantially over the last several hundred years. Studies clearly show an acceleration of forested land converted to cropland starting around the year 1800 (Lambin et al. 2001), which coincides with what historians cite as the beginning of the first industrial revolution beginning circa the year 1780 (Deane 1980; Crafts 1996). There are many other examples of land use/cover conversions (Lambin et al. 2001; Lambin and Geist 2006; Yacouba et al. 2009). Cropland is often converted to residential, industrial or commercial uses (Xiao et al. 2006; Lambin and Meyfroidt 2011). In much rarer circumstances, land is converted back to conditions prior to population/industrial influences (Lambin et al. 2001).

Information pertaining to land cover and subsequent land cover change is important in a wide variety of environmental issues since land cover is a major ecosystem component. These range from the health of local ecosystems to global climatic change, and from human health and well-being to analysis of socio-economic systems. To fully understand change at the global scale one must understand change at the local scale. That

is, most global land cover trends result from the cumulative effect of local land cover changes. One challenge with global scale synthesis of land cover change, however, is that the details about local changes and their drivers are often hidden when examining aggregate global trends. Local changes are often dynamic, rapid and non-linear so that, when aggregated, they do not exhibit any apparent trend. Local changes that may not be apparent at larger scales are nevertheless important because they may reduce the capacity of an ecosystem to adapt to external impacts and its ability to continue functioning as it has in the past (Walker, Salt, and Reid 2006). These abrupt, local changes may be missed in larger scale studies until they grow to a point at which they are apparent at aggregate scales, but after mitigation efforts would be most effective. It remains true, however, that local land cover analyses have limited availability for synthesizing larger scale analyses and so confidence in global or regional results will likely be lower when aggregated. With a limited amount of current land cover analyses at local scales, errors are likely to be more significant in global synthesis studies. Even if local analyses were widely available, the aggregation process risks missing the dynamic, rapid and non-linear changes that are only apparent locally.

Despite the need for local land cover change analyses, there is limited availability of current imagery of a high enough spatial resolution to detect small scale changes. High resolution (1-2 meter spatial resolution) imagery, such as from the *National Agriculture Imagery Program* (*NAIP*) in the United States (Figure 1), generally has 4 spectral bands and has been utilized with some success in separating Ashe-juniper *(Juniperus ashei)* from Live Oak (*Quercus virginiana*) and other common species in central Texas (Ludeke, German, and Scott 2007). Without higher spatial resolution, however, it is

difficult to distinguish individual species entities. Imagery able to detect reflectance patterns of narrow spectral bands, termed hyperspectral imagery, has the potential to differentiate species entities, but satellite-based hyperspectral data will, in most circumstances, have too coarse a spatial resolution to detect individual tree canopies (Asner and Heidebrecht 2010). Conversely, small scale, sub-orbital hyperspectral imagery is currently so cost prohibitive that availability is a problem. When attempting to detect rapid change at local scales this is a significant problem. The solution to this problem is to implement another type of data collection that is easily and quickly obtainable, and that will enhance current locally available data.

Two more recent studies which implemented texture as ancillary data show great promise for texture as an identifier of individual tree species. Yu et al. (2016) successfully combined color, structure and texture into what they refer to as the CTS descriptor. This descriptor was shown to successfully classify high resolution satellite imagery and was especially efficient with very large data sets. Salas, Boykin, and Valdez (2016) also combined texture with spectral data with significant results in the models using texture. This study successfully discriminated sparse vegetation from arid land and further demonstrated that texture can be used successfully with other types of data.

Studies that show the efficacy of texture analysis utilizing grey level co-occurrence matrix (GLCM) have recently been published. Kupidura (2019) demonstrated that the GLCM coupled with granulometric analysis produced texture data that were useful in land use classification. Combining multiple GLCM indices to create a composite band of textural information in pixel based and object-based land cover classification has also produced promising results (Wu et al. 2019; Tassi and Vizzari

2020). Numbisi, Van Coillie, and De Wulf (2019) compared different quantization levels of GLCM data and optical data in delineating cocoa agroforests. They found that data recorded in the 6-bit grey level to be most successful.

Combining GLCM data with SAR and optical data was successful in evaluating damage from a dam break in Uzbekistan. This study exhibited high classification accuracy in identifying inundated vegetation (Tavus, Kocaman, and Gokceoglu 2022). Another successful study combining GLCM with SAR was utilized for agricultural crop classification in differentiating onion from sunflower (Caballero et al. 2020). These and previous studies combined GLCM texture metrics with other types of data and highlights the utility of texture in image classification. What is not said is whether texture alone can be used to classify land cover at equal levels of accuracy as other methods.

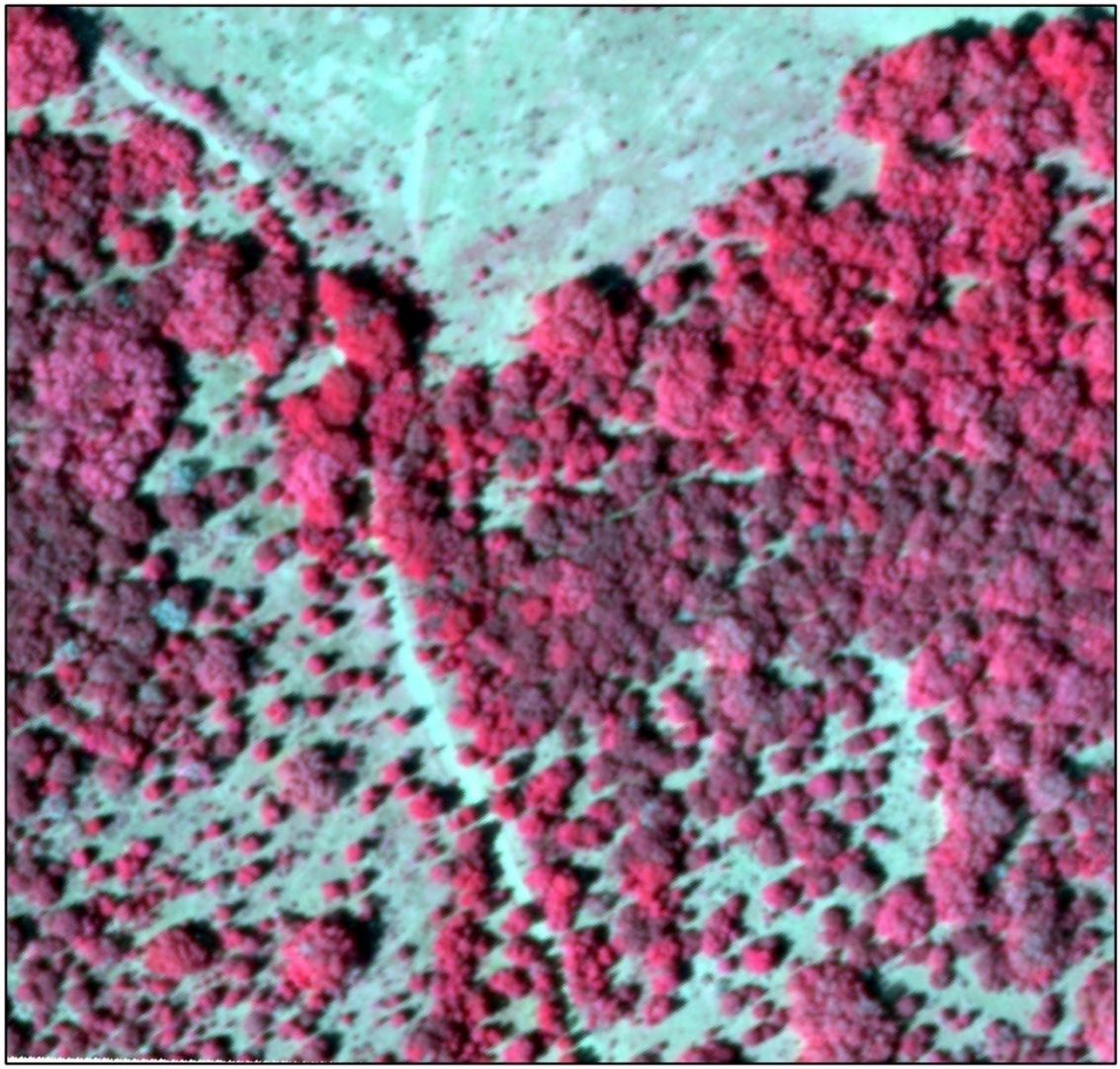

Figure 1 - National Agriculture Imagery Program (NAIP) image showing a portion of the study area within Freeman (Ranch) Center near San Marcos, Texas.

Image Texture for Land Cover Classification

Generally, land cover determination through remote sensing involves spectral analysis of reflected light from a surface target. Human vision, although limited in spectral range, can distinguish between various vegetation types in an aerial photograph or digital image. Nevertheless, there are situations where the reflected energy between two different species is so similar that the two species cannot be differentiated. Methods to distinguish between the two apparently spectrally identical species include 1) examining new wavelength ranges with the intent to discover spectral regions where the signature of the two land cover classes diverge, or 2) increasing the spectral resolution to examine narrower wavelength ranges. While these are possible methods, they are not practical for a remote sensing system where the measurement of specific wavelength ranges is engineered into the sensor. Instead, these options would require a different sensor, with different spectral resolution characteristics. Alternatively, a method that examines other physical characteristics of the land cover could be used.

Identifying the species through physical rather than spectral differences is a viable alternative. Although the spectral signatures of similar species of vegetation may be the same, there may be significant differences in the leaf orientation, density or other physical attributes. One way to quantify these physical differences is to utilize a canopy elevation model to derive a canopy texture model.

Texture plays an important role in human vision for feature recognition and interpretation. Perception of textures provides important details for the analysis of many types of images, including images of the natural environment and biomedical images (Zhu and Yang 1998). The texture of an image scene can be defined as the pixel to pixel

variation in intensity (Jensen 1986; Ulaby et al. 1986; Ngo et al. 2020; Zhang et al. 2022) and has been previously utilized in various LULC studies. Texture in this sense is not related to ground terrain but is instead the local spatial variability of pixel intensities obtained from remotely sensed imagery (Whiteside, Boggs, and Maier 2011; Ngo et al. 2020; Iqbal et al. 2021).

In studying image texture in relation to avian species richness, Culbert and Radeloff (2012) utilized 8 different texture classes, including contrast, correlation, and entropy, and combinations of these variables. They demonstrated that texture was an important tool for explaining avian species richness over broad areas as it measured the degree of ecosystem heterogeneity. Their findings indicated that a biodiverse ecosystem that supported a large variety of avian species had a more heterogenous image texture. Importantly, the authors point out that one limitation of their study was the lack of available imagery during the vegetation phenophase most appropriate for studying avian diversity.

Tuttle et al. (2006) utilized texture in studying habitat use patterns of white- and tan-throated sparrows. The results of this study showed that the white-throated sparrow preferred high-density homogenous habitats such as bog while the closely related tan-throated sparrow preferred areas with greater heterogeneity such as areas adjacent to ponds and meadows. Zhang and Zhu (2011) combined spectral analysis with principal components analysis of gray value textures to produce a land cover classification of suburban areas near Beijing with 90.91% accuracy.

Outside the visible-to-near-infrared wavelength ranges, texture is especially important in RADAR image analysis, where an understanding of different kinds of

texture is essential to proper pre-processing and interpretation. The texture of RADAR images consists of three components: (1) micro-texture or speckle, which appears as grains the same size or larger than the resolution cells, (2) meso-texture or scene texture, which is the natural variation of reflectance from the part of an object facing the sensor to the shadow of the portion of the object facing away from the sensor, and (3) macro-texture, which corresponds to variations in brightness over many resolution cells and usually corresponds to boundaries in larger objects such as roads or geologic features (European Space Agency (ESA) 2013).

Micro-texture or speckle is a phenomenon inherent to the RADAR system used to gather the data. The methodology utilized in this study derives the texture models directly from imagery and does not have the micro-texture component. This is of benefit as the meso- and macro- texture components are the most useful while the micro-texture component is noise that would need to be filtered out.

Ulaby et al. (1986) stated that texture may, in fact, be more useful than image tone in interpreting RADAR images. The tonal variation of individual pixels within image objects were shown to be significant in a classification performed by Ulaby et al. (1986) in their study using RADAR images for LULC detection. Using tone alone a classification accuracy of 75% was achieved. When combining tone and texture the accuracy exceeded 90%.

Implementing texture as a measure of the physical characteristics of a tree canopy has challenges like those of spectral imagery. Canopy texture is based on a canopy elevation model and creating an elevation model that captures the variability of within-canopy height, leaf orientation and leaf density depends on the resolution of available

imagery. These physical characteristics will only be apparent with a very high spatial resolution image. For example, existing elevation models at 1 to 30 meters are too coarse to observe canopy texture so a method to obtain finer resolutions must be implemented. Figure 2 shows a section of a 1/9 arc second (~3 meter) DEM from central Texas. When comparing the NAIP image of the same area, individual tree crowns cannot be detected in the DEM. The NAIP image is at a resolution where individual crowns are visible, but even NAIP imagery has insufficient spatial resolution to detect canopy texture characteristics.

Aerial imagery or DEM's with the resolution to detect the texture of tree crowns is not something that is generally available without considerable effort and expense. An alternative is to create a DEM using overlapping stereo images. The first requirement to create a DEM at a very high resolution using overlapping imagery is to use a high-quality camera flown at a low altitude (< 150 meters) so as to produce high spatial resolution imagery. The only option currently available that meets these requirements is to use an Unmanned Aerial System with a pre-programmed flight path and altitude.

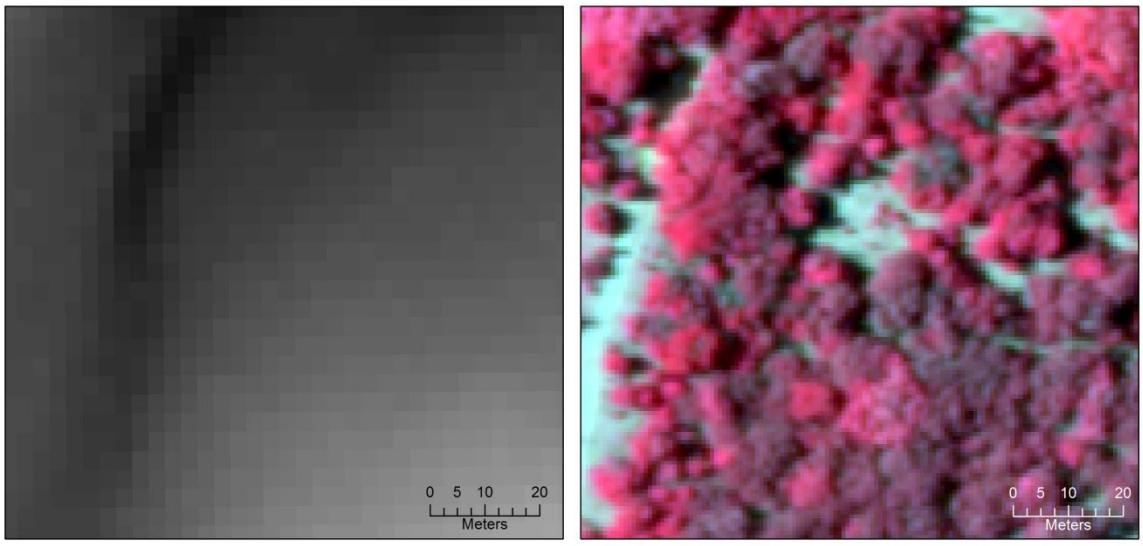

Figure 2 - National Elevation Dataset (NED) 1/9 arc second (3 meter) resolution DEM and NAIP imagery at 1-meter resolution of the same portion of the study area.

Manual and Automated Photogrammetry

The beginnings of stereo photography can be traced back as far as 280 A.D. when Euclid was the first to recognize that depth perception was the result of the eyes receiving two slightly different images. Much later, in 1611, Kepler's *Dioptrice* was published and included descriptions of the projection theory of human stereo vision (Thakare, Arbal, and Shahade 2011). Parallax refers to the relative change in position of an object that is due to differences in the angle at which the object is viewed. After Kepler's work, several methods were discovered that induced the human brain to perceive depth from two-dimensional, overlapping images. Anaglyphic 3D originated circa 1850 and utilized colored filters to introduce to each eye an image of the same scene, but taken from different viewing angles. One hundred years later during WWII, photo analysts used stereoscopes (devices used to view overlapping photographs in 3D) to observe enemy installations taken by photo-reconnaissance aircraft.

Aerial photography has well-known radial distortions that can be used to measure distances and heights from overlapping photograph pairs in a process called photogrammetry (Lillesand, Kiefer, and Chipman 2004). Using the focal length of the mapping camera and the flying height of the plane on which the camera flew, the scale of the photography can be determined, and horizontal measurements made on the photography can be converted to ground distances. Measuring object heights is more involved than horizontal measurements and requires that an analyst align the centers of two photographs (i.e., their principal points) with the centers of their neighboring photographs (i.e., their conjugal principal points) to determine a flight line, and then manually measuring the degree of displacement (i.e., the absolute parallax) of an object

in both overlapping photographs. The absolute parallax is used to convert object heights from photograph units to actual ground heights.

Using additional parameters that describe the camera orientation relative to the ground, manual photogrammetric principles are used to orthorectify images and create photo-mosaics and elevation models (in analog or digital format). Interior camera orientation parameters include precise measurements of the camera shape (e.g., the focal length and the camera width and length, as measured between fiducial marks encoded on the photographic images). Exterior orientation parameters include the horizontal coordinates (X, Y) and altitude (Z), as well as the 3D orientation (Ω, Φ, and K—also known as roll, pitch and yaw) of the camera, at the time of image acquisition. Tie points are points manually identified on multiple overlapping images that corresponds to matching objects on the ground, and ground control points are tie points for which XYZ ground coordinates are known. Tie points enable parallax height measurements across the images from which are derived surface elevations and ground control points enable creation of a georeferenced image mosaic and digital surface model.

Structure from Motion (SfM) is an automated photogrammetric imaging technique for creating three dimensional objects from overlapping two dimensional images. Where SfM differs from traditional photogrammetry is that SfM does not require that the exterior camera orientation parameters or tie points be known *a priori*. Instead, camera positions and orientations are derived by automatically identifying common points in the overlapping imagery using one of a set of algorithms known as automatic feature detection algorithms (Tareen and Saleem 2018). By tracking these points through multiple overlapping images taken at various locations and angles, the X, Y and Z

coordinates, and the Ω, Φ and K 3D orientation angles of the camera can be calculated in relative space (Westoby et al. 2012). Once interior and exterior orientation parameters have been derived, digital image mosaics and surface models are created. If ground control points are available, these products can be accurately georeferenced (Westoby et al. 2012).

While SfM is relatively new in the field of remote sensing it has been utilized in many studies in recent years. In a study concerning the role of SfM in physical geography, Smith, Carrivick, and Quincey (2015) highlights applications of SfM to monitoring glacier movement, quantifying soil loss and gully erosion, observing and tracking lava movement and landslide displacement, monitoring coastal recession, surveying fluvial morphology including submerged surfaces, characterizing rock outcrops and quantifying aboveground forest biomass. SfM studies specific to vegetation are increasingly common. In a study of dryland vegetation Cunliffe, Brazier, and Anderson (2016) were successful in showing that SfM could accurately model vegetation height.

Lidar

Elevation data can be generated using Light Detection and Ranging (lidar), a remote sensing technique that uses laser light to measure distances from a sensor to surface targets (ground, building, tree, etc.). The first lidar systems worked by transmitting one or more pulses of laser light from a sensor to the Earth's surface. This system continues to be the most common system today, but systems that transmit a continuous waveform of laser light are becoming increasingly common (Mallet and

Bretar 2009). The transmitted laser light reflects off a surface target and returns to the sensor, where the difference in time from transmission to return is recorded (Dong and Chen 2017). Multiplying the speed of light by half the time difference produces the distance to the surface target. The distance datum, coupled with a GPS and Inertial Measurement Unit (IMU) to record the exact XYZ location and the 3D orientation of the sensor, allow for a precise determination of the location and elevation of the surface target. Multiple surface targets are measured this way through the forward motion of the sensing platform and by continuously changing the incidence angle of laser light. This *point cloud* of measurements often has sub-meter point density (depending on the aerial platform flying altitude and laser pulse density) and is the raw data produced by a lidar system.

Current systems transmit and receive either multiple pulses, or a continuous waveform, of laser light. The first return is from a high elevation surface (i.e., the target closest to an airborne sensor) and the last return generally is the ground (i.e., the target furthest from an airborne sensor). Intermediate returns represent targets at intermediate elevations and the distribution of multiple returns is correlated with the physical object being measured. Most returns are from the uppermost surface targets, but even some points are usually returned from the ground for surface targets with gaps in their aerial coverage (e.g., trees). For example, the distribution of multiple returns in a forest ecosystem corresponds to the structure (e.g., distribution of leaves) in individual tree canopies (Froidevaux et al. 2016; McCarley et al. 2017; Wiggins et al. 2019). Importantly, the class of object represented by each point in the point cloud is unknown until further analysis is performed.

Lidar analysis usually involves ground filtering, point interpolation and the determination of object heights (Dong and Chen 2017). The purpose of ground filtering algorithms is to classify lidar points as ground or non-ground (Meng, Currit, and Zhao 2010; Martínez Sánchez et al. 2019). Directional, morphological, interpolation-based and segmentation-based ground filtering algorithms are each appropriate for unique environmental conditions (Meng, Currit, and Zhao 2010; Ramola, Shakya, and Pham 2020; Fonseca et al. 2021). These algorithms scan the point cloud for point-to-point differences in elevation and determine thresholds of elevation change that ground and non-ground surfaces.

Interpolation of a gridded elevation raster using the entire lidar point cloud produces a Digital Surface Model (DSM) that is usually of little value because it averages multiple returns over a ground sample distance. Instead, the filtered ground points are interpolated to create a Digital Terrain Model (DTM). The non-ground points are used to determine objects heights above the surface of the terrain surface. Depending on the elevation and geometric distributions of point heights above the terrain, points can be further classified into unique surface objects (buildings, trees, etc.) (Meng, Currit, and Zhao 2010).

The last decade has seen much growth in lidar technology with applications ranging from forestry, to the cryosphere, to urban growth and more (Dong and Chen 2017; Liao, Zhou, and Yang 2021). Lidar data and analysis excel at producing ground and surface elevation datasets, even in areas of dense tree canopy coverage, but require great expense for equipment purchase, maintenance, and data storage and processing.

Comparing lidar and Structure from Motion

Wallace et al. (2016) and Mlambo et al. (2017) indicate that while SfM produces an overall denser canopy point cloud than lidar, lidar still excels in the production of an accurate ground model. Both studies indicated better accuracy from lidar in the representation of the bare earth model. Wallace et al. (2016) found a difference greater than 0.5m between lidar and SfM-based digital terrain models due to SfM's limited ability to penetrate a vegetation canopy and register ground points in heavily vegetated areas.

Due to the terrain being occluded at various viewing angles, Wallace et al. (2016) indicated a point density of 0.5 ground points per square meter in the SfM ground point cloud. Canopy height models were adversely affected due to the accuracy of the ground model as these measurements utilized ground height in their calculation. One other advantage that SfM holds over lidar besides canopy point density is the recording of RGB values. This allows the point cloud to be displayed in a manner similar to a photograph which is very advantageous when using the point cloud to delineate features.

Advances in computer vision algorithms, such as parallel bundle adjustments which utilize the latest in graphic processing unit (GPU) technology allows for matching distinct objects found in hundreds or thousands of overlapping photographs taken from varying angles, have made SfM a viable option for creating digital surface models (Wallace et al. 2016; Deliry and Avdan 2021; Liao, Zhou, and Yang 2021). By extension, SfM appears to be an excellent technique for acquiring hyperspatial resolution elevation models of individual tree canopies that can be used to determine canopy texture.

Image Classification Algorithms and Techniques

Unsupervised classification is used when an analyst has little or no information on the number, type or spectral variability of land-cover classes in a study area. The first step in unsupervised classification is to apply a clustering algorithm that identifies pixels of similar spectral value. One common algorithm in remote sensing analysis, the Iterative Self-Organizing Data Analysis Technique (ISODATA), requires that an analyst input an initial number of desired clusters to find before iteratively assigning pixels to spectrally similar clusters of pixels. Cluster assignments are iteratively refined until reaching an analyst-defined number of iterations or a threshold of unchanged pixel assignments is reached. The second step in unsupervised classification is for an analyst to manually apply a semantic label to each of the algorithmically defined spectral clusters that correspond with each land-cover classes of interest.

Supervised classification automatically assigns a semantic label to pixels based on training data provided by an analyst that consists of manually assigned class labels for a selection of pixels of known value. An algorithm is then selected that will learn from the training data how to correctly assign the correct label to all image pixels. One of the most common supervised classification algorithms is the Maximum Likelihood Classifier (Yacouba et al. 2009). This method applies probability theory in determining class assignments by using the mean, variance and covariance to determine to which class a pixel belongs in the training data. A Bayesian probability function is applied to the variance and covariance matrices for each of the classes of the training data, resulting in a set of multi-dimensional ellipses defining class boundaries. All image pixels are then classified by the trained algorithm, resulting in an exhaustive image classification.

Pixel-based image classification techniques assess each pixel in an image individually and assign that pixel to a land-cover class using an unsupervised or supervised technique that incorporates multiple spectral measurements per pixel. Ancillary information (e.g., a digital elevation model) may be used in pixel-based methods, but each pixel is considered in isolation—neighboring pixels are not examined when classifying a pixel. Pixel-based classification techniques have been extensively used, but recently object-based techniques have become prevalent because they show significant improvements in accuracy, especially with high spatial resolution remotely sensed images (Myint et al. 2011).

Object-based classification techniques consider the spectral information of a neighborhood of pixels as well as other neighborhood parameters like texture and shape in the classification process, thereby increasing the ability to discriminate between different objects that have similar spectral signatures (Zhou and Troy 2008). Blaschke (2010) found broad agreement that current Object-Based Image Analysis (OBIA) builds on previous edge detection and feature extraction techniques, and argued for a new merger between GIS and previous image processing techniques that he called Geographic Object Based Image Analysis (GEOBIA).

When performing GEOBIA, image pixels are segmented into superpixel objects—groups of neighboring pixels with a high degree of spectral homogeneity. Nevertheless, individual pixels in a segment may exhibit some heterogeneity due to factors such as shading or variations in sun angle (Whiteside, Boggs, and Maier 2011). Each segment is treated as a distinct ground object with unique spectral, spatial and texture attributes. The spectral attributes for each object are usually the average

reflectance of all pixels in each spectral band comprising the segmented object. A variety of spatial attributes can also be calculated, including the area and perimeter of the object and the concavity, semi-major axis, and orientation, for example. Texture attributes are measures of the pixel-to-pixel variation in spectral response within the segmented object. Together the spectral, spatial and texture attributes are used to assign each segmented object to a land-cover class using an unsupervised or supervised algorithm. Analysis of segmented objects eliminates problems faced in pixel-based classification where the variability in neighboring pixels that belong to the same ground object leads those pixels to be erroneously assigned to different land-cover classes.

There appears to be disagreement in the available literature over how and when object-based classification outperforms pixel-based classification. Many publications claim that object-based classification has greater potential for classifying higher spatial resolution imagery than pixel-based methods (Willhauck 2000; Mansor, Hong, and Shariff 2002; Oruc, Marangoz, and Buyuksalih 2004). However, Dingle Robertson and King (2011) found no statistically significant difference between the two methods in their study using McNemar's non-parametric test for proportional difference (de Leeuw, Verschure, and van Liere 2006), although visual inspection indicated the object-based approach incurred less significant error in the larger regions of homogeneous cover and performed better in temporal analysis of land cover change (Dingle Robertson and King 2011). Niemeyer and Canty (2003) claim that object-based classification has greater potential for detecting change in higher resolution imagery. Castillejo-González et al. (2009) found that an object-based method out-performed five pixel-based supervised classification algorithms (parallelepiped, minimum distance, Mahanalobis Distance

Classifier, Spectral Angle Mapper, and MLC) for mapping crops and agro-environmental associated measures. Based on their reference data, Gao and Mas (2008) achieved far greater accuracy in mapping 12 land cover classes using an object-based versus a pixel-based approach (83.25% and 46.48%, respectively), while the object-based methodology used by Gao and Mas (2008) outperformed both MLC and nearest neighbor pixel-based methods in mapping cover using SPOT 5 (10 m spatial resolution) data. However, the authors noted that after smoothing filters were applied to the imagery, the accuracy of the pixel-based methods increased while object-based accuracies decreased.

III. DATA & METHODOLOGY

Study Area

Freeman (Ranch) Center is located approximately 7 kilometers northwest of San Marcos, Texas on the eastern edge of the Texas Hill Country and Balcones Escarpment (Figure 3). The ranch covers an area of 1702 ha (4,204 acres). It is a working ranch that is operated by Texas State University and is available for research in fields such as ecology and agriculture. The land cover consists of areas that are primarily pastureland with Plateau Live Oak *(Quercus virginiana* var. *fusiformis)* and Ashe juniper *(Juniperus ashei)* savannas in the uplands that grade gradually into closed-canopy woodlands. The variation of the land cover makes it ideal for the proposed study. Predominant soils of the ranch are the Comfort and Rumple series which are moderately deep upland soils. Each of these soils is of a stony clay mixture which is ideal for growth of Ashe-junipers (Baccus et al. 2000). The topography of the ranch is generally hilly with several steep canyons and streams. Elevations range from 204 to 287 meters.

According to the Köppen Climate Classification system the Ranch has a humid subtropical environment (Cfa) which is characterized by hot, humid summers (July mean temperature of 30°C) and generally cool to mild winters (January mean temperature of 10°C). Mean annual precipitation averages approximately 900 mm but is characterized by great seasonal and annual variation (Earl, Dixon, and Day 2006; U.S. Climate Data Center 2021).

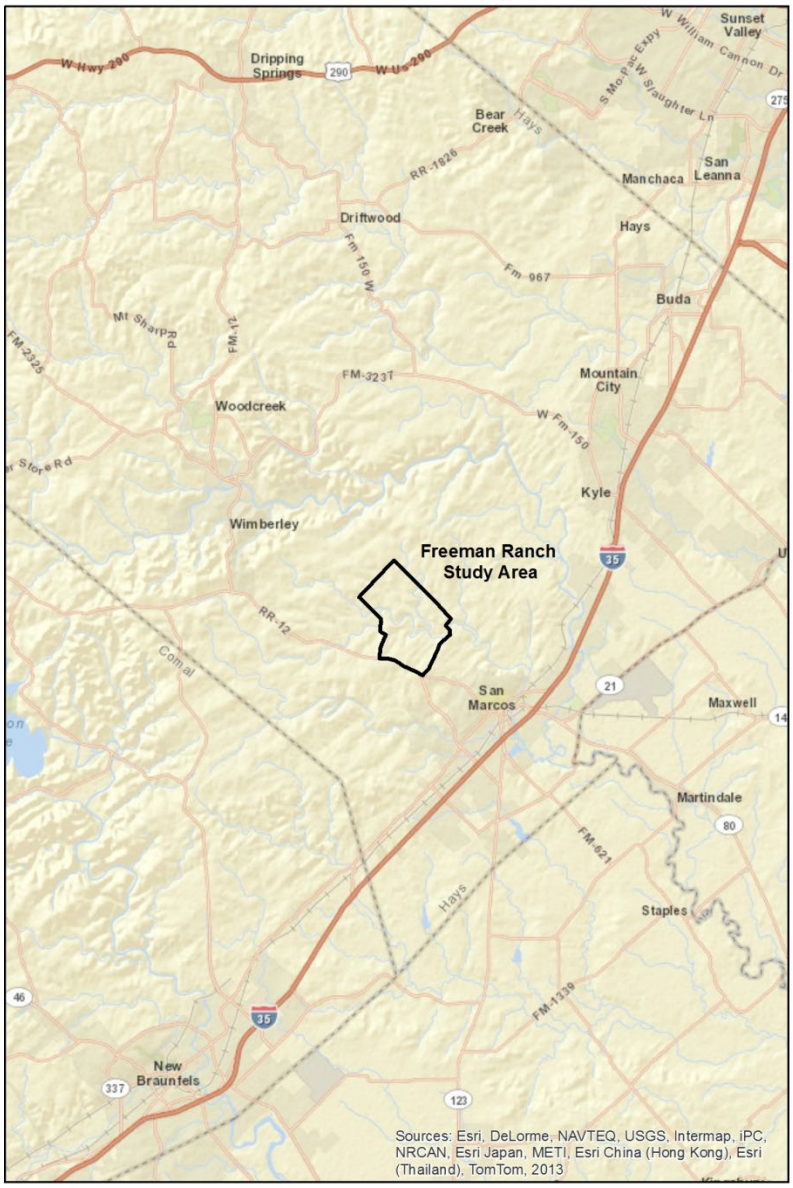

Figure 3 - Polygon indicates location of study area located 11 kilometers Northwest of San Marcos. Scale 1:300,000. (ESRI, 2013)

The diversity of the ranch is evident when listing the ecosystems located within the ranch boundaries. The Texas Ecological Systems Classification Project (Texas Parks and Wildlife 2021) lists 27 distinct ecosystems on Freeman Ranch (Table 1, Figure 4).

The specific study area is located in the southeastern third of the ranch. Air navigation sectional charts indicate the northern portion of the ranch intersects an approach cone for the San Marcos Municipal Airport. For safety and efficiency reasons it is advisable to stay in the southernmost section of the ranch.

After evaluating several potential study areas, a plot of approximately 53 hectares was selected at Freeman Ranch in San Marcos Texas (Figure 5). The criteria used for selecting this area were accessibility and variability. The accessibility allows for easy access for both data gathering and ground truthing. Variability of the site is good as it contains a variety of species. Species found on the site during the initial survey were primarily Plateau Live Oak (*Quercus virginiana)* and Ashe Juniper (*Juniperus ashei),* and secondarily Honey Mesquite (*Prosopis glandulosa),* Netleaf hackberry *(Celtis laevigata),* and Cedar elm *(Ulmus crassifolia).* It was determined that Honey Mesquite, Netleaf Hackberry and Cedar Elm were so scarce and dispersed that this research will only classify Plateau Live Oak and Ashe Juniper. The terrain is variable ranging from 214 meters ASL to 242 meters ASL with the highest point in the northwest corner and the lowest in the southeast. The study area is bisected from north to south by Sink Creek which is the ephemeral headwaters of the San Marcos River.

Table 1. Texas Ecological System Classification Project ecosystems located in Freeman Ranch.

Ashe Juniper Slope Forest
Ashe Juniper / Live Oak Shrubland
Ashe Juniper Motte and Woodland
Deciduous Oak / Evergreen Motte and Woodland
Floodplain Deciduous Shrubland
Floodplain Hardwood / Ashe Juniper Forest
Floodplain Hardwood Forest
Floodplain Herbaceous Vegetation
Floodplain Live Oak Forest
Live Oak Motte and Woodland
Live Oak Slope Forest
Native Invasive Deciduous Woodland
Native Invasive Juniper Woodland
Native Invasive Mesquite Shrubland
Oak / Ashe Juniper Slope Forest
Oak / Hardwood Motte and Woodland
Oak / Hardwood Slope Forest
Post Oak Motte and Woodland
Riparian Ashe Juniper Forest
Riparian Ashe Juniper Shrubland
Riparian Deciduous Shrubland
Riparian Hardwood / Ashe Juniper Forest
Riparian Hardwood Forest
Riparian Herbaceous Vegetation
Riparian Live Oak Forest
Savanna Grassland
Shin Oak Slope Shrubland

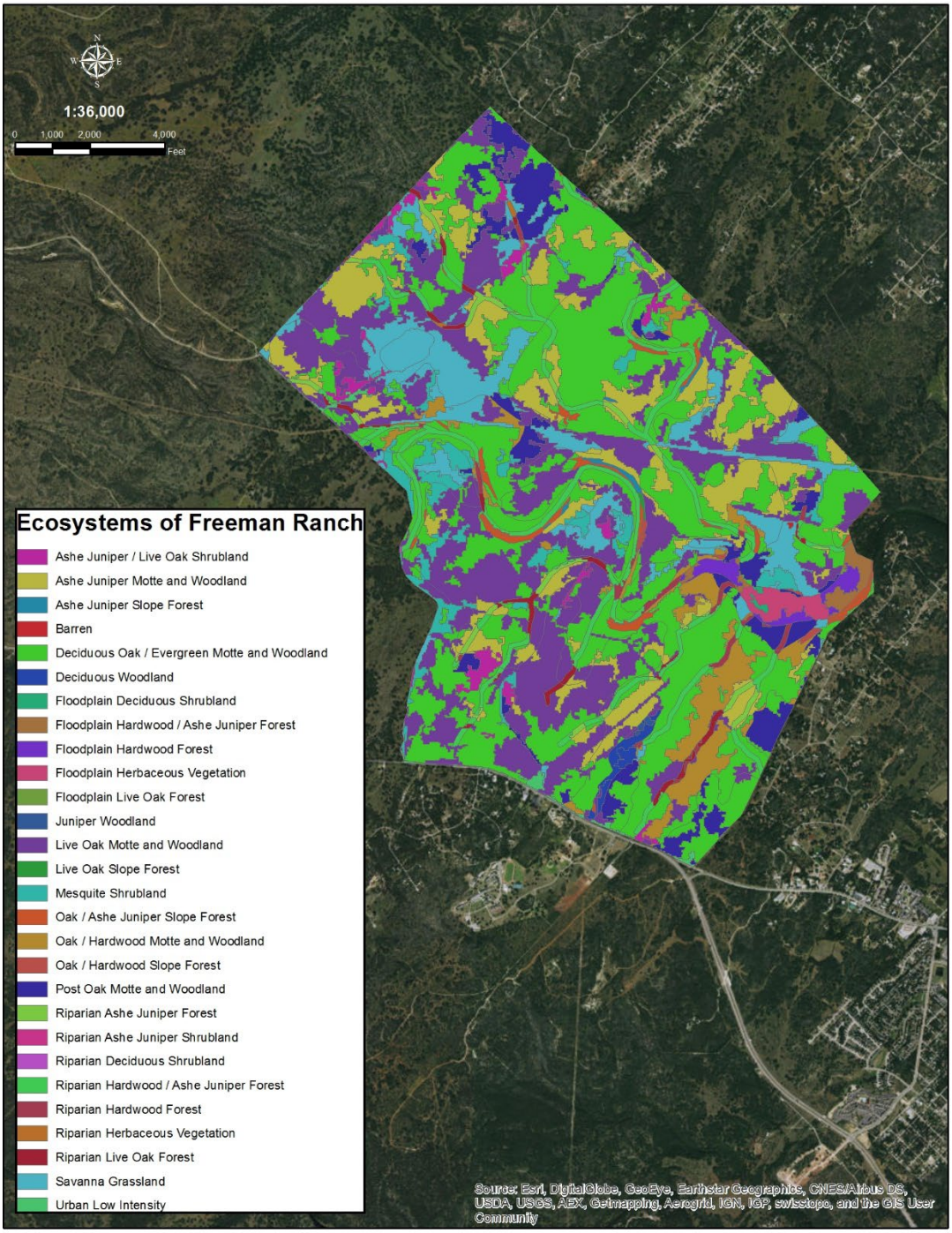

Figure 4 - Ecosystems of Freeman Ranch (Texas Parks and Wildlife 2021)

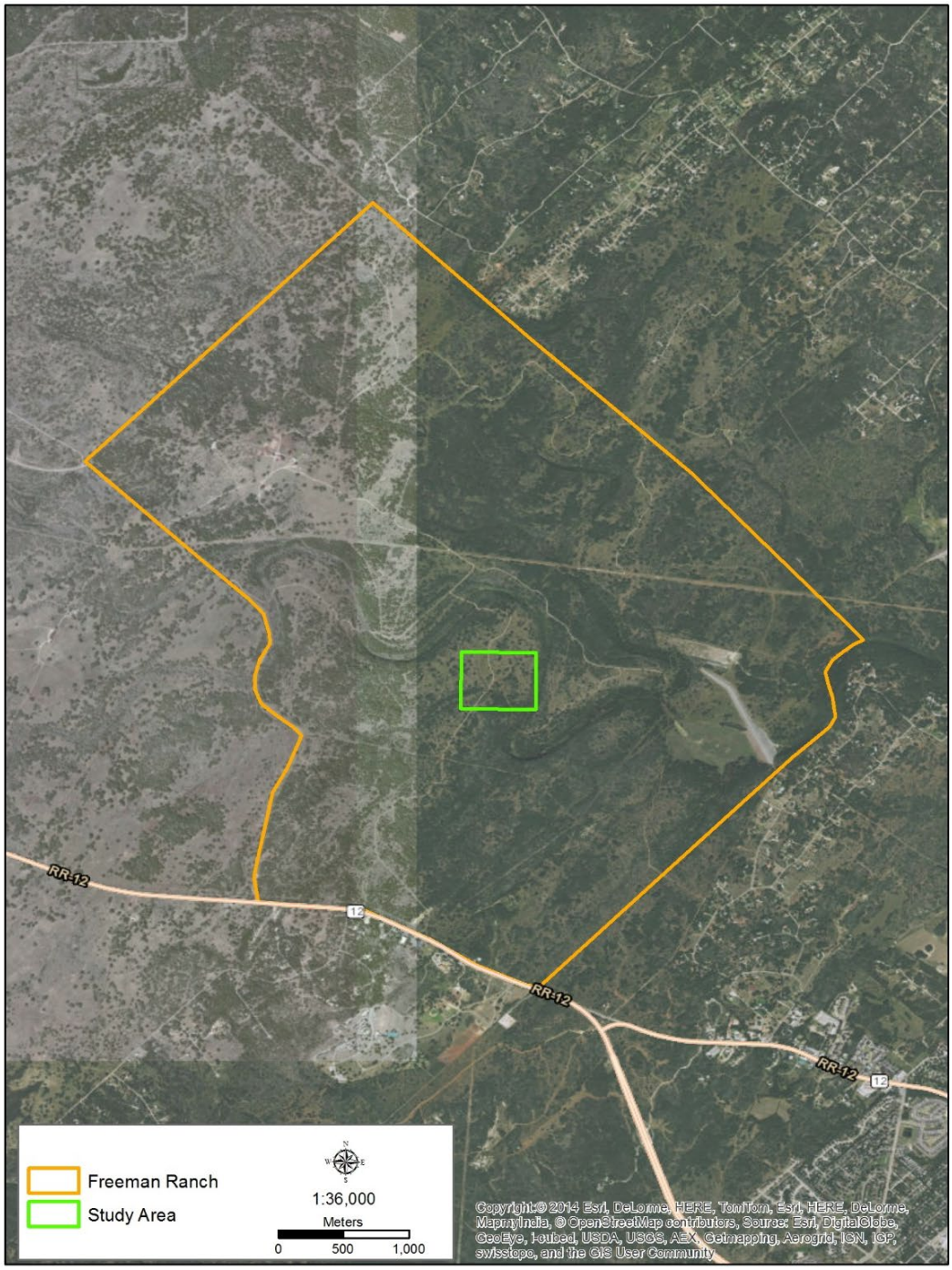

Figure 5 – Study area within the Freeman Ranch Boundary

Data Collection of Tree Canopy Elevation Textures

An Unmanned Aerial System (UAS) was used to gather primary image data in the spring and summer of 2015 under clear skies and near solar noon to minimize shadows. Reducing shadows was important because shadows obfuscate the actual land cover and, of special relevance to this study, hide the textural variations in smaller trees adjacent to larger trees. Collected imagery was mosaiced into a seamless RGB image mosaic and a 3D pointcloud and digital surface model were created by utilizing the stereoscopic qualities of the overlapping imagery and SfM algorithms. Then, the texture of the canopy elevations (as an indicator of canopy structure) was derived from the DSM. An initial segmentation was performed on the RGB mosaic to delineate forested areas that served to refine the extent of the study area and made possible the classification of tree types based on their canopy texture. Two classifications were made from the forested study region as follows: (1) The canopy texture model was combined with the RGB image mosaic and classified using GEOBIA techniques, and (2) The RGB image mosaic was classified using the pixel-based, supervised Maximum Likelihood classifier. For comparison, a third classification was performed on National Agriculture Imagery Program (NAIP) imagery using NDVI incorporated into GEOBIA techniques and in the same forested study region as the other classifications. Once the classifications were completed, ground truthing took place and statistical tests were performed to assess accuracy.

UAS Image Collection

Five ground control points (GCP) were placed in the study site prior to UAS image data collection to aid in mosaicking and georeferencing the imagery obtained. The

GCP targets consisted of orange foam squares measuring 1 x 1 meter with a 12-inch diameter circle painted in the middle. The precise XYZ coordinates of the GCP's were measured using an Ashtec MM100 GPS and differential correction techniques to an accuracy of < 1 cm (Figure 6).

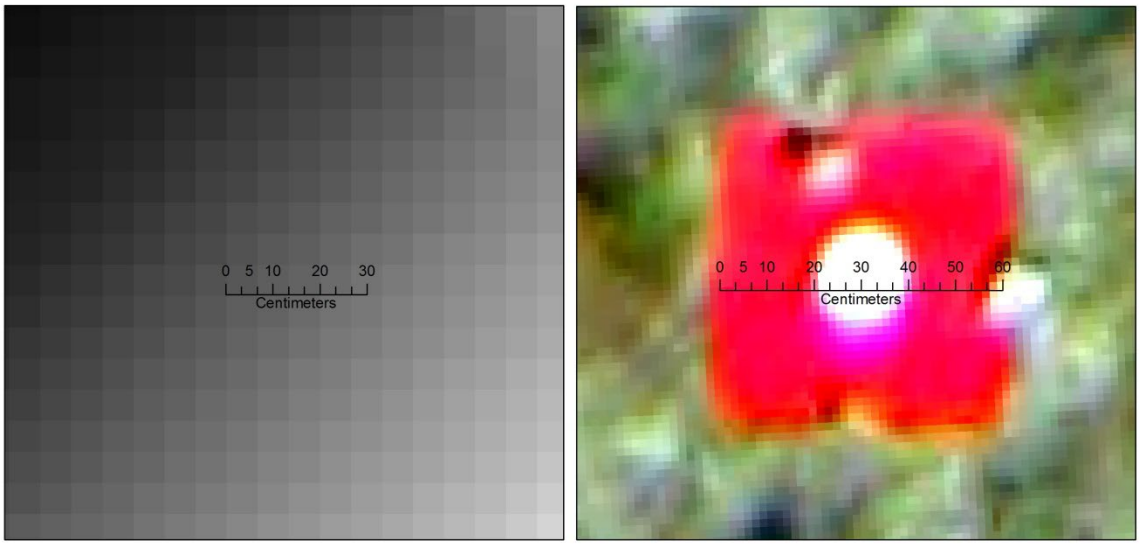

Figure 6 - DEM (left) created from UAS imagery indicating approximately 7.5cm resolution. Right image shows ground control target in same location.

Two aerial systems were considered for this study: one rotorcraft and one fixed wing. The two systems had very different flight characteristics and utilized cameras with very different specifications. The rotorcraft was built by 3D Robotics with a Gopro 3+ Black mounted on a 2D gimble. The fixed wing Areohawk was manufactured by Hawkeye UAS and carries a Sony Nex7 camera. Specifications for each platform can be viewed in the Appendix. After evaluating data collected by both systems it was decided to utilize the imagery from the Areohawk. While the X8 flew at a much lower altitude (increasing the pixel resolution) it also used a much lower quality camera. Imagery from the AreoHawk showed better resolution even when flying over three times the altitude of the X8. The GoPro imagery from the X8 platform also required processing to remove the fisheye effect inherent in that camera which added to the complexity of the process.

The aircraft was always required to be within the line of sight of the drone operator per FAA regulations, even though the airspace utilized was below the regulated airspace for manned traffic. Pre-flight safety checks were an important part of drone operation (just as they are with manned aircraft) and included the following items:

1. Check aircraft propellers, body, and control surfaces for damage.
2. Power up ground station and load flight plan.
3. Check flight plan parameters such as waypoints, speed and altitude.
4. Power on hand control transmitter.
5. Power up aircraft.
6. Check wireless link between hand control and aircraft.
7. Check wireless link between ground station and aircraft.
8. Upload mission to aircraft.
9. Check throttle, and control surface links between manual controller and aircraft.

Upon passing all of these checks the aircraft was ready for launch.

Ground control software, software installed on a portable computer that maintains constant contact with the UAS while it is in operation, was used to upload the flight plan

to the UAS and issue commands to it while it was in flight. Flying altitude and the amount of photographic overlap were important considerations of the flight plan because they have a direct relationship with the resolution of the objects in the images—higher altitudes lead to coarser spatial resolution images and lower altitudes increase the likelihood of motion blur being introduced to images. The flight altitude was programmed to stay just below the 400-meter maximum altitude dictated by law for radio-controlled aircraft in the United States and the photographs in this study had a minimum of 50% overlap obtained using a back-and-forth (mowing the lawn) flight path. The camera shutter was manually controlled from the ground and was adjusted depending on the speed of the aircraft. It was determined that approximately one photo per second was the ideal rate at which to take photos.

The ground control software monitored the UAS's precise flight path and recorded the camera location and attitude (i.e., its 3D rotation along X, Y and Z axes) for each photograph taken (Table 2, Figure 7). This data allowed the SfM software to accurately place measured object points in their proper location and orientation in space. Without attitude data, the resultant geometric accuracy of the images would be spatially most accurate near the GCP's and would degrade with distance away from the GCP points. With the attitude data, the resultant images had improved geometric fidelity. The photographs and the camera logs containing the camera location and attitude data were saved on completion of the photography mission.

Table 2 – Sample of flight log data created by autopilot. The columns that are used in the SfM process are CLat (Camera Latitude), CLon (Camera Longitude), CAlt, (Camera Altitude), CPi (Camera Pitch), CRol (Camera Roll), CYaw (Camera Yaw), and CFOV (Camera Field of View).

Photo	Epoch	Time	SLR	TLat	TLon	AAT	Azi	Dpr	CLat	Clon	CAlt	CPi	CRoll	CYaw	CFOV
26	48270	15322875	0	29.93294	-97.9883	0	0	90	29.93293	-97.9882	1427.5	1.2	-1.36	179.39	70
27	48321	15323075	0	29.93341	-97.9882	0	0	90	29.93338	-97.9882	1415.7	-0.33	-1.49	-175.38	70
28	48371	15323275	0	29.93387	-97.9882	0	0	90	29.9338	-97.9881	1409.1	-0.42	-3.76	-168.43	70
29	48421	15323475	0	29.93436	-97.9879	0	0	90	29.93427	-97.9879	1397.3	-3.34	1.65	-170.92	70
30	48471	15323675	0	29.93484	-97.9876	0	0	90	29.9347	-97.9878	1388.5	-5.04	5.6	-172.93	70
31	48521	15323875	0	29.93534	-97.9877	0	0	90	29.93514	-97.9877	1386.2	-5.58	0.06	-173.74	70
32	48571	15324075	0	29.93574	-97.9875	0	0	90	29.93564	-97.9876	1389.4	-3.69	1.14	-171.85	70
33	48621	15324275	0	29.93612	-97.9875	0	0	90	29.93607	-97.9875	1394.4	-1.19	-0.24	-172.38	70
34	48671	15324475	0	29.93648	-97.9873	0	0	90	29.93648	-97.9874	1396.3	1.11	0.89	-173.88	70
35	48721	15324675	0	29.93697	-97.9873	0	0	90	29.93696	-97.9873	1390.1	-0.37	0.54	-174.63	70
36	48771	15324875	0	29.93747	-97.9871	0	0	90	29.9374	-97.9872	1394.4	-2.15	1.09	-170.94	70
37	48821	15325075	0	29.93797	-97.9872	0	0	90	29.93784	-97.9871	1398.3	-3.19	-2.73	-170.25	70
38	48871	15325275	0	29.93825	-97.9868	0	0	90	29.93832	-97.987	1397.6	2.2	3.63	-173.77	70
39	48921	15325475	0	29.93876	-97.9872	0	0	90	29.93874	-97.9869	1396	1	-10.18	-173.69	70
40	50561	15340050	0	29.94004	-97.9881	0	0	90	29.94016	-97.988	1348.8	-4.66	1.41	12.95	70

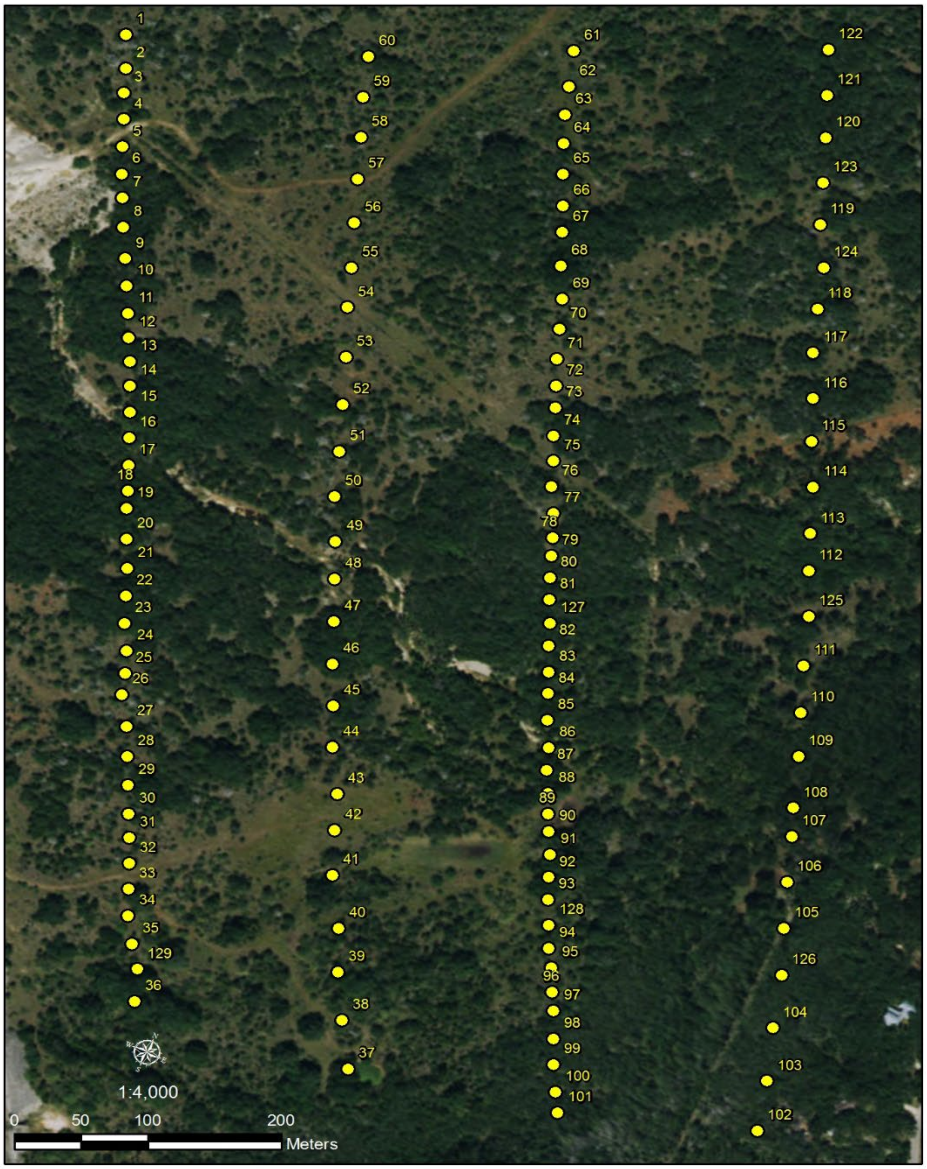

Figure 7 – Example of flight path and photo points overlaid on aerial imagery. Any points that fall outside of the known flight path should be eliminated.

Structure from Motion Processing

Before SfM processing could occur, each photograph was manually evaluated and any photograph that was undesirable was eliminated along with its corresponding record in the camera log. Examples of eliminated photos included those that were out of focus or taken as the aircraft was banking. The raw imagery was then color balanced in Adobe Photoshop and converted to the RAW image format preferred by the SfM software. The camera log files were imported into Microsoft Excel where the appropriate photograph filenames and file types were associated with their corresponding X, Y, Z coordinates and roll, pitch and yaw camera orientation angles. The ground control points were added into a second Excel spreadsheet and saved in the same way as the log files. The workflow then used to create the mosaic and point cloud is shown in Figure 8.

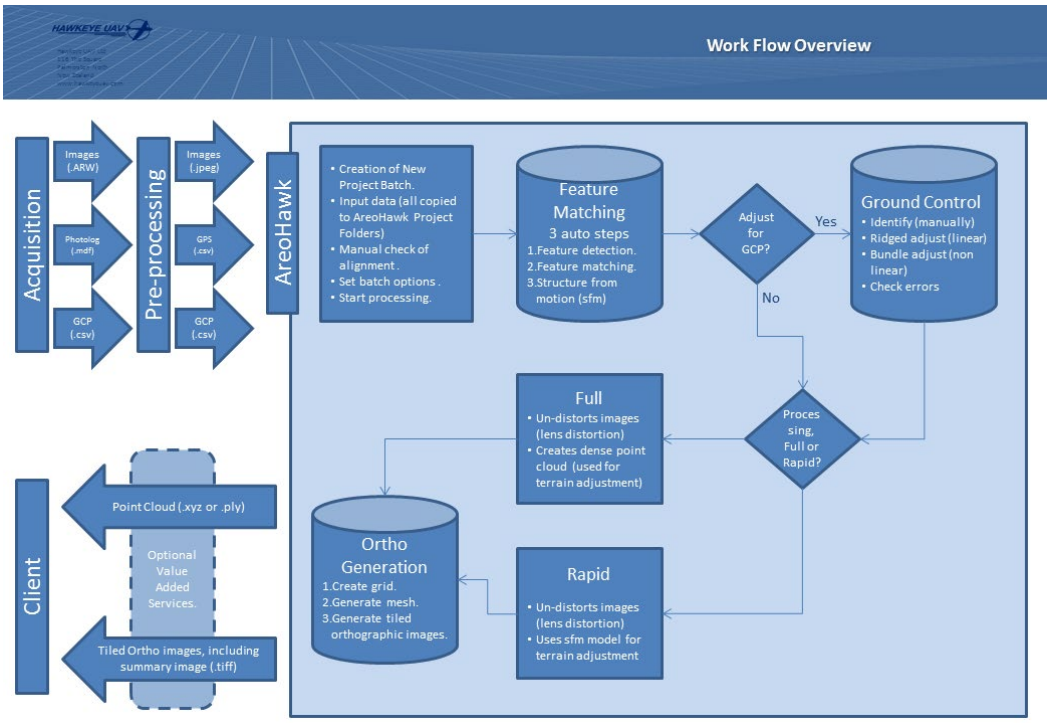

Figure 8 – Data Processing Workflow

Color-balanced drone imagery was processed using SfM techniques found in the Agisoft Photoscan software and included the bundle adjustment procedure, image mosaic creation, and extraction of the 3D point cloud. The tie points created in the bundle adjustment procedure were identified by aerial triangulation of corresponding features tracked from image to image that allowed for the derivation of the camera position in relation to each tie point. Coordinates of matching photograph points were determined relative to the different camera positions and added to a point cloud database. Because this study collected georeferenced ground control points prior to image data collection, the resultant image mosaic and point cloud were georeferenced in 3D space and ready for integration with other geospatial data. The point cloud created through the SfM process was then converted to a digital surface model (DSM) using ArcGIS 3D Analyst. Because of the high resolution of the digital camera, the relatively low flying altitude, and the accuracy of photograph placement using the SfM technique, a resolution of less than 10cm was achieved. This hyperspatial DSM was then used to create a measure of tree-canopy texture that was incorporated into the supervised classification processes, as described in the next section.

Land-cover Classifications and Comparisons

Three classification methods were used for this study, 1) a texture-based GEOBIA of the canopy structure derived from drone imagery, 2) a spectral-based supervised classification of the drone imagery using the maximum likelihood algorithm, and 3) an NDVI-based classification using National Agriculture Imagery Program (NAIP) digital aerial photography. Trimble eCognition Developer software © was used for the GEOBIA

models and ERDAS Imagine was used for the spectral model. Classifications from the different methods were compared to test whether there was significant improvement in the accuracy of the texture-based GEOBIA classification compared to the other classification methods.

GEOBIA and The Gray Level Co-occurrence Matrix

GEOBIA consisted of segmenting the image mosaic into groups of image pixels called super-pixels or objects, calculating object attributes including the mean spectral response and image texture based on the Gray Level Co-occurrence Matrix (GLCM) for each segmented object, and classifying the objects into land-cover classes. The image mosaic was segmented using the eCognition software's multi-resolution segmentation process, which required 3 analyst-defined parameters: scale, shape and compactness. There is no agreed upon set of scale, shape and compactness values for optimal segmentation in all cases, nor any heuristics for selecting values for a particular use case (Kavzoglu and Yildiz 2014; Akar and Gormus 2021; Bai et al. 2021). Instead, these values are set by trial and error until a satisfactory segmentation has been reached, as determined by the analyst. Scale is an abstract value that determines the maximum possible change in heterogeneity that results from merging neighboring objects and roughly corresponds to average object size. Small (large) scale parameter values tend to result in smaller (larger) sized objects, on average. The shape parameter value is a real number in the range [0, 1] that determines the balance between spectral heterogeneity and geometric shape in determining segments. Small (large) shape parameter values tend to result in objects primarily defined by their spectral (geometric) characteristics. The

compactness parameter value is a real number in the range [0, 1] that determines the balance between smoothness and compactness metrics of segment geometries. Smoothness and compactness metrics are calculated as follows:

$$compactness = \frac{l}{\sqrt{n}}$$

$$smoothness = \frac{l}{b}$$

where l is the perimeter of a potential image object, n is number of pixels in the object, and b is shortest possible border length of a box bounding of the object. Small (large) compactness parameter values tend to result in objects that are less (more) circular in shape. The resultant smoothness and compactness values were 0.3 and 0.5, respectively, which resulted in the image segments displayed in Figure 9.

A two-step segmentation process was followed in this research. The first application of image segmentation was used to delineate broad land cover classes to identify forested areas. In this step, the aim was to distinguish between other land cover classes (e.g., grasslands, roads, buildings, and shadows) and forested areas. Oversegmented forest object boundaries were dissolved to delineate a single multi-polygon representation of forested areas, and these forested areas became the refined study area where the influence of tree canopy texture on classification accuracy could be tested using object- and pixel-based classification methods (i.e., all three methods proposed in this research). The second application of image segmentation was used in the first and third GEOBIA classification efforts that included segmentation of individual

trees or tree clusters of the same species into unique image objects, object attribution (including a GLCM texture measure or NDVI, depending on the classification method), and the classification of objects into either the Live Oak or Ashe Juniper land cover classes.

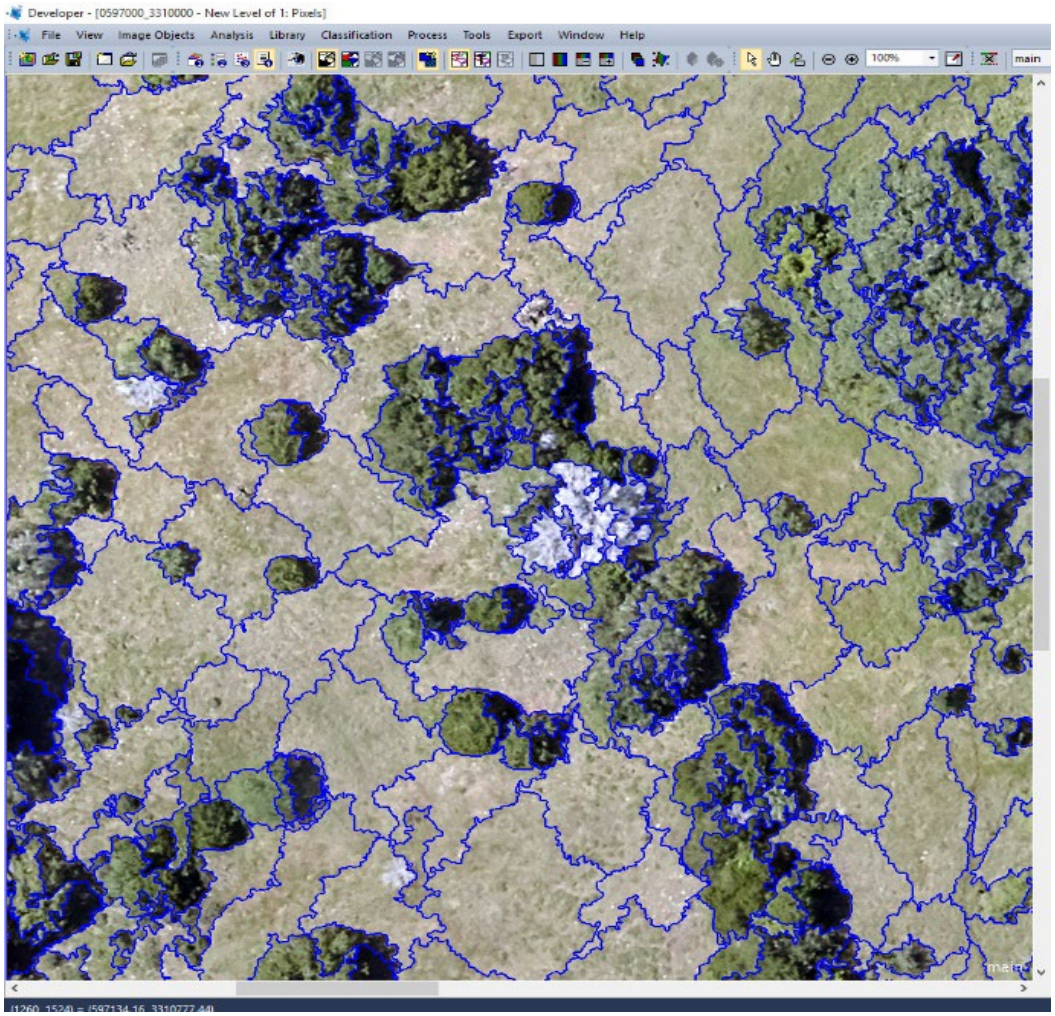

Figure 9 – Results of the GEOBIA segmentation process using Trimble eCognition. The segments created were used to (1) delineate the forested-region study area for all classification methods, and later to (2) delineate individual trees or clusters of trees of the same species within the forested study area using the first and third classification methods.

The Gray Level Co-occurrence Matrix (GLCM) represents the joint probability of occurrence of 2 values at given distance and orientation offsets (Rampun, Strange, and Zwiggelaar 2013; Akar and Gormus 2021). It is a statistical method that measures texture by tabulating how often different combinations of pixel brightness values occur in an image (Hall-Beyer 2017). This statistical relationship is generally measured between reference pixels and their immediate neighbor pixels in a specified direction and orientation, making it a second order relationship (Hall-Beyer 2017; Weigand et al. 2020). While third order and higher calculations are possible, they are computationally intensive and do not yield significantly improved results (Hall-Beyer 2017). The purpose of using the GLCM in this research is to examine the role of canopy structure in land-cover classification, where canopy texture is a proxy for canopy structure, Therefore, the DSM created as described in the previous section was added as a 4^{th} layer to compliment the 3 RGB layers of the drone imagery mosaic in the GEOBIA process. The GLCM required 8-bit integer values, so the floating-point elevation values were first normalized to the digital number (DN) range [0..255] and was referred to as the normalized DSM (nDSM). The steps outlined in the following paragraphs were made for a 5x5 kernel successively centered on each pixel of the normalized image to produce an output surface texture image.

An empty GLCM with cells for all possible DN combinations in the kernel was created (e.g., [0,0], [0,1], [0,2], [1,0], [1,1], [1,2], [2,0], [2,1] and [2,2] for a kernel with 3 DN values). Each pixel in the kernel (called a reference pixel) was compared to its neighbor pixel and a tally of each DN combination was kept in the GLCM matrix. For example, if the reference pixel had a DN value of 1 and its neighbor had a DN value of 2, the

tally of the 1st row and 2nd column of the GLCM matrix would increment by 1. This procedure continued until all pixels were evaluated. The tally was repeated by switching reference and neighbor pixels to create a GLCM matrix that was symmetrical around the diagonal. Matrix values were then converted to probabilities by dividing each cell by the total number of possible DN combinations in the matrix. Finally, the correlation texture measure was calculated from the GLCM probability matrix and assigned to the pixel at the kernel center in the output surface texture image. The correlation texture measure was calculated as:

$$correlation = \sum_{i,j=0}^{N-1} P_{i,j} \left[\frac{(i - \mu_i)(j - \mu_j)}{\sqrt{(\sigma_i^2)(\sigma_j^2)}} \right]$$

where $P_{i,j}$ probability matrix, N is the number of rows or columns, μ_i and μ_j are the means of row *i* and column *j*, and σ_i^2 and σ_j^2 are the variances for row *i* and column *j*. The resulting image had pixel values that ranged from 0 to 1, with 0 being a smooth textured surface and 1 being a highly variable texture surface.

The mean red, green, blue and texture attribute values were calculated for each segmented object in the dataset using zonal statistics and were used to classify the objects into land-cover classes. A selection of segmented objects was manually made and used to train the nearest neighbor classification algorithm to recognize the selected land-cover types. This was an iterative process that allowed for continuous improvements in classification accuracy. Once classification of objects into vegetation types was completed, final tree classes were exported as classified vector objects for accuracy assessment and comparison to other classification data and methods.

Pixel-based, Supervised Maximum Likelihood Classification

A multi-spectral (i.e., no canopy texture measure) classification was preformed using the drone-based imagery and a supervised maximum likelihood classifier (MLC) in ERDAS Imagine. The MLC is a parametric statistical technique that assumes normally distributed training data for each spectral band of each land-cover class. Based on knowledge of the study site obtained through field surveys, individual polygons were digitized around samples of each land-cover type and mean class vectors and the covariance matrix was calculated from the pixel values for each spectral band of each land-cover class. The training data was reviewed, and new training polygons were created as needed to ensure the data were normally distributed. These polygons were grouped using the ERDAS signature editor to create a representative signature for each land-cover type (Figure 10). The classified raster image (Figure 11) was then converted to a vector GIS file for accuracy assessment and comparison to the other classification methods.

The training data was used to calculate the probability of each pixel in the image belonging to a land-cover class, according to the following equation

$$p(X|w_i) = \frac{1}{\sqrt{2\pi^n}\sqrt{|V_i|}} exp\left[\frac{-1}{2}(X - M_i)^T {V_i}^{-1}(X - M_i)\right]$$

where $p(X|w_i)$ is the probability that unknown vector X (the RGB pixel values) belongs to land-cover class w_i, n is the number of bands (3 in this case), ${V_i}^{-1}$is the inverse of the covariance matrix and $|V_i|$ is the determinant of the covariance matrix. The class w_i with the greatest probability is the class assigned to the output pixel—it becomes the land-

Class #	Signature Name	Color	Red	Green	Blue	Value	Order	Count	Prob.	P	I	H	A
1	live oak		0.388	0.429	0.437	9	23	6631	1.000	✔	✔	✔	✔
2	juniper		0.380	0.403	0.287	11	33	1180	1.000	✔	✔	✔	✔

Figure 10 – Table showing RGB signatures of study area tree classes.

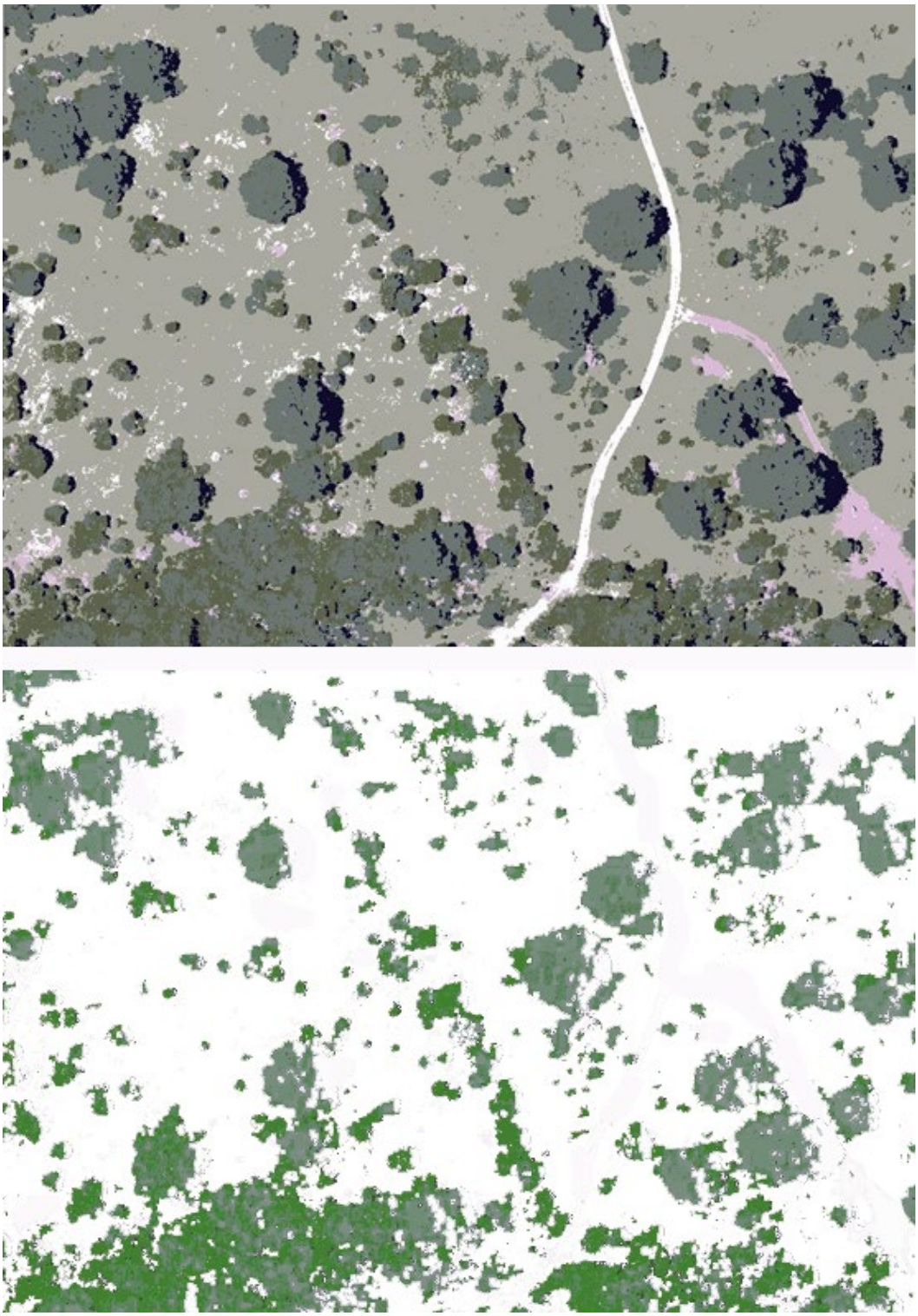

Figure 11 – Drone imagery classified using the maximum likelihood classifier (top) was clipped using the forest canopy segments to include only forested areas (bottom).

cover class for that pixel. The mean class vectors (M_i and covariance matrix (V_i) were estimated from the training data.

NDVI analysis using NAIP Imagery

A third classification was made with which to compare the previous drone-based imagery classifications. This third classification was done using readily available U.S. National Agricultural Imagery Program (NAIP) imagery with high spatial resolution (1 meter) and low spectral resolution (4 VNIR bands). A significant limitation of NAIP imagery is that its spatial resolution is too coarse to do texture-based analysis of tree canopies, but in this case, it serves as a baseline against which canopy texture-based classifications can be compared.

GEOBIA was used for the NAIP classification, including segmentation, attribution and classification of segmented objects. Therefore, the methodology for this section is the same as for the previous GEOBIA section with the exception that texture was not calculated as an attribute. Instead, the Normalized Difference Vegetation Index (NDVI) was calculated and used as an attribute for segment classification, in addition to the mean red, green and blue band values per segment. Calculation of NDVI required a NIR band so it was not possible to use the drone imagery for NDVI analysis, but using it here with NAIP imagery was a best practice for imagery with a NIR band. Analyst-selected objects were used as training data for an MLC classification to identify tree types. Classified vector segments were exported for accuracy assessment and comparison to the other classification methods.

Accuracy Assessment

Accuracy assessment was a multi-step process to quantify thematic accuracy of the UAS-based RGB/texture classification using GEOBIA, the UAS-based RGB image classification using a pixel-based Maximum Likelihood Classifier, and the NAIP-based RGB/NDVI classification using GEOBIA. Assessing thematic accuracy of classified pixels and objects required creating a set of point reference features through a ground survey of the study area. The land cover classes confirmed in the ground reference survey were used to populate an error matrix—a cross-tabulation table used to compare reference data to classified pixels. Various accuracy metrics were derived from the error matrix to assess the accuracy of each classification separately and then pair-wise statistical comparisons were made between pairs of classifications. These methods are discussed in further detail below.

A stratified random sampling design, based on the work of Lo and Watson (1998), was used to conduct the ground reference survey. In their study, Lo and Watson evaluated the accuracy of five sampling designs for a land cover classification of the Okefenokee Swamp, including the simple random sample, stratified random sample, random systematic sample, stratified systematic unaligned sample, and random cluster sample designs. They classified a Landsat TM image and compared samples obtained using each of the different sampling designs to a detailed reference land cover map rasterized to the same resolution as the TM image. Kappa coefficients and Z scores indicated that the stratified random sampling and stratified systematic unaligned methods produced the highest accuracies, but the chi-square goodness of fit test comparing the stratified random sample with the reference data was the only comparison in which the

null hypothesis (i.e., no difference between samples) was accepted. That is, the stratified random sample was the most accurate sampling technique, and it was selected for use in this research to provide ground reference points.

Selecting the number of the reference points per class was a balance between acquiring a sufficiently sized sample for statistical validity and the difficulty of acquiring reference data in the field (Foody 2002; Congalton 2004). Importantly, a sample that is too small may result in the inability to detect differences that are large and important, and a sample that is too large may result in any non-zero off-diagonal value being statistically significant (Foody 2009). While care must be taken to obtain a properly sized sample, there is no single, globally accepted method for determining the sample size and a combination of methods are often used (Foody 2009). Congalton and Green (2019) stated that as a rule of thumb sample sizes should have a minimum of 50 samples per class. The size selected for the accuracy assessment reference set in this research was 85 points per tree class (170 total points per classification method) which exceeds Congalton and Green's rule of thumb and, according to binomial probability theory and multinomial probability theory (Snedecor and Cochran 1967; Olofsson et al. 2014), provided 7.4% and 8.4% confidence intervals at the 0.05 significance levels, respectively. A number of points proportional to the areal coverage of each classified land cover type were randomly placed within each land cover strata.

A unique stratified random sampling was made for each of the forest classes derived from each classification method performed in this research (i.e., ground reference samples were not reused in for different classification methods). The actual tree types found at each sampling point were confirmed by field verification and an error matrix

was created. Accuracy metrics derived from the error matrix included overall accuracy, user's accuracy and producer's accuracy. Kappa is an often-used metric that attempts to correct for chance agreement between classified and reference pixels, but Olofsson et al. (2014) recommend against its use because (1) it tends to underestimate the probability that a random pixel is classified correctly, (2) it bases its estimates of random agreement on the marginal proportions of map area (which are not randomly distributed), and (3) it is redundant because it is so highly correlated with overall accuracy. We did not report it in this research for the reasons outlined above.

Overall accuracy is the percentage of correctly classified reference pixels and was calculated by dividing the sum of the correctly classified reference pixels (i.e., the cells on the error matrix diagonal) by the total count of reference pixels. The distribution of off-diagonal reference pixels gave further insight into the accuracy of individual land cover classes. Dividing the total number of correctly classified pixels in a class by the total of that class' reference data (i.e., the column total) yielded the producer's accuracy—the probability that the reference pixel was classified correctly. Dividing the total number of correctly classified pixels in a class by the total of that class' classified data (i.e., the row total) yielded the user's accuracy—the probability that a classified pixel corresponds to that land cover class in the field. Subtracting the producer's and user's accuracies from 100 yielded errors of omission and commission, respectively.

Lastly, the accuracies for each classification type were analyzed for significant differences using a multinomial comparison called the Z score (aka standard score). The Z score was calculated as

$$Z = \frac{|p_1| - p_2|}{\sqrt{{s_1}^2 + {s_2}^2}}$$

Where *p* represents the proportional accuracy of each map (sample size/correct observation) and *s* represents the standard deviation. First, the Z score was calculated for significance between the remotely sensed data and the ground reference data and second, a test for significance between each of the remotely-sensed results was performed. The final test indicated if there was a significant improvement between the different data and methods of classification.

IV. RESULTS AND DISCUSSION

An error matrix is shown for each classification type: (1) UAS-based RGB/texture classification using GEOBIA, (2) UAS-based RGB image classification using a pixel-based Maximum Likelihood Classifier, and (3) the NAIP-based RGB/NDVI classification using GEOBIA. The overall, producer's, and user's accuracies are reported. The accuracies of each classification are ranked to assess the relative utility of each method with special attention to the texture-based method.

Overall, Producer's and User's Accuracies

The initial survey of the study area identified five tree species: Live Oak, Ashe Juniper, Cedar Elm, Net Leaf Hackberry and Mesquite. Upon completion of the image processing, analysis and ground truthing, it was found that the number of trees species other than Live Oak and Ashe Juniper was so small and dispersed as to be indistinguishable from the two dominant species. Live Oak and Ashe Juniper were the only classes analyzed and reported on. One-hundred seventy ground reference points were randomly distributed in each land cover class in number proportional to the areal coverage of each land cover class.

Table 3 displays the error matrices resulting from the three classification algorithms. The columns correspond to the ground reference data and the rows correspond to the classified data. Cross referencing each cell shows the number of correct identifications and misidentifications for each class. The first row in the first table shows that of 62 objects classified as Juniper, 11 were actually Live Oak. The first column of

the first table shows that out of 72 Juniper reference pixels, 21 were erroneously classified as Live Oak. These matrix tallies lead to producer's and user's accuracies of 70.83% and 82.26%, respectively. The rest of the tables can be interpreted the same way. The overall accuracy is calculated by dividing the number of correctly classified observations by the total number of reference points. Based upon the overall accuracy, the texture-based GEOBIA model ranked highest with 81.18% overall accuracy. Producer's and user's accuracies were also acceptable. The spectral-based maximum likelihood classification has the second highest overall accuracy (78.24%) and the NDVI-based GEOBIA had the lowest overall accuracy (75.29%).

Table 3 – Error matrices for the three classification methods. Overall accuracies are shown to the right of each error matrix. User's accuracy (UA) and producer's accuracy (PA) are shown for each row and column, respectively, in the error matrix.

A. Texture-based GEOBIA

Classified \ Reference	Juniper	Live Oak		UA	
Juniper	51	11	62	82.26%	
Live Oak	21	87	108	80.56%	
	72	98	170		Overall
PA:	70.83%	88.78%			81.18%

B. Spectral-based MLC

Classified \ Reference	Juniper	Live Oak		UA	
Juniper	45	15	60	75.00%	
Live Oak	22	88	110	80.00%	
	67	103	170		Overall
PA:	67.16%	85.44%			78.24%

C. NDVI-based GEOBIA

Classified \ Reference	Juniper	Live Oak		UA	
Juniper	50	18	68	73.53%	
Live Oak	24	78	102	76.47%	
	74	96	170		Overall
PA:	67.57%	81.25%			75.29%

Table 4 is a comparison of the rankings in accuracy between the overall results and the Z score of each classification. Importantly, these results show Z scores for all three tests that are well above 1.96 indicating that these methods show results that are significantly better than random. These results support the hypothesis that canopy texture is an indicator of individual tree species and that its use improves on commonly used reflectance-based methods.

Table 4 – Classification significance levels. Z-scores and their significance levels are shown for each classification at the 95% confidence level.

Classification Algorithm	Overall Accuracy	Z score	Result (95% confidence level) if Z is above 1.96
Texture-Based Drone	81.18	10	Significant
Spectral-Based Maximum Likelihood	78.24	8	Significant
NDVI-Based OBIA	75.29	7	Significant

Pair-wise Comparisons

Table 5 compares the texture-based results to the maximum likelihood results and the NDVI results. Results of the tests indicate that the texture-based method is not significantly different at the 95% confidence level than the other methods of classification. The Z statistic for the texture-based drone method vs. NDVI- based method yielded a 1.32 Z statistic (1.96 being the target) at an 81% confidence level. Results of the texture-based drone method vs. maximum likelihood yielded a Z statistic of 0.67 at a 49% confidence level. The overall accuracy of the texture-based GEOBIA classification was 2.94% higher than the spectral-based classification (which is considered the baseline, or "standard", classification method). However, the difference in overall accuracy was not statistically significant at the 95% confidence level. Certainly, one interpretation of this finding is that the texture-based GEOBIA does not provide an improvement over standard classification methods and refutes the premise of this research that hyperspatial DEMs collected with a UAS will improve classification accuracies. By this logic, similar classification accuracies can be obtained using NAIP imagery and supervised classification using the maximum likelihood decision rule. This logic suggests that the overhead incurred by using UAS to derive hyperspatial DEM data that can measure tree canopy texture may not be as advantageous as initially thought. Alternative explanations, however, offer greater insight into the findings.

Table 5 – Comparative classification analyses. Z-scores of the comparative analyses between classifications showing significance results at the 95% confidence level.

	Z statistic	Confidence level	Result (95% confidence level)
Texture-based vs. maximum likelihood	0.67	0.49	NS
Texture-based vs. NDVI	1.32	0.81	NS

While the difference between the texture-based GEOBIA classification and the spectral-based classification was not significantly different at the 95% confidence interval, there is still the higher overall accuracy to consider. And even though there is less confidence attributed to that difference, the 2.94% higher accuracy of the texture-based GEOBIA classification cannot be ignored. Moreover, that this accuracy is achieved when texture is the only unique attribute on which the segments are classified, suggests that texture is an important distinguishing ecological attribute of tree species that can be assessed with drone-based imagery—and perhaps only with drone-based imagery.

In fact, recent evidence suggests that the incorporation of multiple ancillary data sources, including texture, improve classification accuracies. Yu et al. (2016) explored the capabilities of texture analysis with a model called Color-Texture-Structure (CTS). This model incorporated both texture, spectral and structural elements into the model. Structure in this model refers to the co-occurrence of objects such as an island being in co-occurrence with surrounding water. The results of the CTS study showed significant improvements in classification accuracies by using color, texture and structure in combination. Salas, Boykin, and Valdez (2016), in a study of vegetation in the Pamir Mountains in Tajikistan, performed an analysis of the spectral curve called the Moment Distance Index (MDI) and used it as ancillary data in combination with texture analysis. In this case, the comparison was between texture alone and texture and MDI in combination. They found significant improvements in classification accuracy with the addition of MDI. It is interesting to note that the results of Salas, Boykin, and Valdez (2016) approximate those of this dissertation. Additionally, Husson, Ecke, and Reese (2016) produced overall accuracy results of 75% using similar methodologies on RGB

drone imagery, which further suggests that the methodology employed in this dissertation is comparable to related methodologies.

Reconsidering Texture as an Ancillary Data Source

The findings of this study, and the recent evidence cited above, suggest that certain assumptions of this research should be reconsidered, including the role of canopy structure, the selection of a texture measure, and spatial and temporal variations in texture.

Canopy Structure

The canopy structure of the tree species in this study were the basis for creating the classifications. Without significant differences in the canopy structures, a classification algorithm could not discern one species from another by studying their textures. It is likely there are tree species with similar canopy structures which may be indistinguishable using this model, but in such cases additional ancillary data could be added to the model to discern differences in the species.

A canopy can be defined as the above ground portion of a plant community or crop, formed by the collection of individual plant crowns (Norman and Campbell 1989). Specific to this study, the "canopy" is the portion of the overall tree canopy that is viewable from the air and thereby part of the structure used when creating the DSM and subsequent models.

The structure of the canopy is made up of a variety of components. The smallest elements are the leaves. The leaves of the two species examined in this study are very

different in terms of shape and density. The Live Oaks have flat and oval leaves while the Ashe Juniper's are needle-like—typical of an evergreen. Density refers to how tightly clustered the leaves are in a typical tree representative of this species. The lower the density the greater the gaps in the canopy which results in a greater variation of light to dark as reflectance changes from a leaf face to a shadow. These differences in leaf density lead to changes in tree canopy textures that are unique to each tree species. Finally, crown size is an important indicator of tree species—clusters of individual trees of a given species can produce a pattern that is discernable from one species to another. These tree canopy characteristics visible to a remote sensor are important to consider in devising accurate methodologies to distinguish between tree species.

Scale Texture

If a person were to view a typical example of a Live Oak or an Ashe-Juniper at close range (from any side or above it), it would be easy to tell them apart. Besides differences in the green tone of the leaves, each tree has a different shaped canopy and different leaf structure, as noted previously. Additionally, the bark or the size of branches may be different between the species. The challenge in automating what a person can detect is that a person is able to detect small differences that may not be detectable by a computer algorithm. There are at least two reasons why a computer algorithm may perform poorer than a person: (1) an algorithm only classifies what the user explicitly instructs the algorithm to classify, and (2) the data used may be of a resolution that is incongruent with the pattern trying to be detected. For example, a person might see slight variations in the shapes of the leaves. One leaf might be completely rounded where the other ends in a point. These subtle differences would not be enough to change the texture pattern at the

scale this model utilizes and would not be practical as the resolution required for such detection would make the file size of the imagery unmanageable. Unique texture patterns may emerge, however, if multiple, aggregated, pixels resolutions are examined. That is, texture indices based on coarser resolution DEMs may be unique to a particular species.

During the GEOBIA process, the object size is something that can be set as one of the working parameters. As can be seen in Figure 9, the segmented object size is often roughly the size of an individual tree crown, but is equally often larger in size where groups of trees are very clustered—the entire cluster is a single segmented object. Visual analysis of the image shows that some tree species tend to cluster together while others are more widely dispersed. While this pattern is not canopy texture measured at the pixel-to-pixel level (as was done with the GLCM in this dissertation), these patterns of growth (clustered vs. dispersed) could be considered a type of image texture attributable to a broader spatial scale. Incorporation of this type of spatial arrangement in the classification process could potentially be an additional ancillary data source.

In contrast to the textures that become apparent at a broad spatial scale, some texture characteristics may only become apparent at finer spatial scales. For example, the bark color or texture, or the arrangement of branches (during a leaf off period) may be unique to a tree species and could possibly be assessed with a texture-based method. This, too, could be an additional source of ancillary data.

Temporal Texture

Temporal texture refers to how the texture pattern varies as a function of plant phenology—the seasonal cycle of the plant. Two species that have the same texture pattern at time A might have very different texture patterns at time B. For example, Live Oaks in this study area lose their leaves in the spring rather than the fall. In this case, the texture pattern will be vastly different in the springtime, when the Live Oaks are either dropping leaves or growing new ones while other leaf bearing trees are in the middle of a different phenophase. The opposite will take place in the fall when the Live Oaks are fully leafed and other trees are dropping leaves. This is a scenario where texture patterns will be very different at particular times of the year. Ashe juniper are a true evergreen and consequently, can be easily distinguished from Live Oak during the spring when the oaks have shed their leaves.

Other Potential Applications of Hyperspatial Texture-based Land Cover Classification

The findings and conclusions of this research suggest that hyperspatial digital canopy models are accurate indicators of individual tree species. Canopy structure, scale texture and temporal texture each play a role in the ability of texture metrics to facilitate the classification process. While the environment (Freeman Ranch) in which this research took place has unique characteristics that will likely only be matched in nearby locations, the findings were sufficient to suggest texture could be equally valuable in other environmental conditions. In the paragraphs below, I briefly explore how texture could play a role in other regions of Texas. No doubt classifications from regions across the globe could also benefit from texture analysis.

Invasive or non-native species are a large problem in many places. Salt Cedar *(Tamarix ramosissima)* is a non-native plant invading habitat in states such as California, Arizona, New Mexico, Texas, Colorado, Utah and Wyoming (Lovich 2022). Part of eliminating invasive species is the ability to quickly identify where these species are growing and stressing native plant and animal life. Salt Cedar is problematic in that it consumes large quantities of ground water thereby denying many native plants adequate water. Salt Cedar are shrubby with green wispy foliage. Their canopy structure is unique compared to the native broad-leafed tree that grow in proximity to Salt Cedar, much like the canopy differences between the Ashe Juniper and Live Oak species studied in this dissertation. With the likely difference in texture between the Salt Cedar and proximate native tree canopies, a study of identifying this invasive species would be a worthy endeavor.

Invasive species are a serious threat in the Trans-Pecos region of West Texas. Salt Cedar is, again, one of the species of concern in this area including but not limited to Chinaberry trees *(Melia azedarach),* Mimosa *(Albizia julibrissin)*, and Yellow Star Thistle *(Centaurea repens).* A common trait in many of these invasive species is their ability to consume available water which is not only what makes them successful in these areas but also what makes them so dangerous to native species. Another concern of these water hungry, non-native species is by consuming so much water from the surrounding areas, they create overly dry ground conditions leading to additional dust blown into the atmosphere. West Texas is a prime area for wind and solar energy generation. Dust accumulation on solar panels is a big problem in this windy part of the state. By

controlling the invasive species and returning the native plants and grasses would play a big part in limiting the dust in the atmosphere.

The Trans Pecos desert of Texas is likely to be another area of slower than average change as was discussed in the introduction of this dissertation. The areas of change are likely to be more spread out making them more difficult to detect with common, low resolution remotely sensed data. As previously mentioned, Salt Cedar has a similar structure to that of Ashe Juniper, making the methodology in this study a good fit for this area. Many of these invasive plants produce distinctively shaped buds and flowers during in their phenological cycle. These changes to the plant structure would very likely be detectable with the texture-based GEOBIA method test in this study.

V. CONCLUSION

The variety and magnitude of land cover changes across the globe occur because complex social, economic, and demographic conditions drive a multitude of local landscape changes. A constant challenge for the remote sensing of land cover changes is to obtain an accurate depiction of where, and at what pace, change is occurring. Orbital and suborbital remote sensing systems are designed with specific spatial, spectral, radiometric and temporal resolution characteristics that constrain the types of changes that can possibly be detected. Certain resolution characteristics are better suited for detecting particular types of landscape conditions or changes. Remotely sensed, hyperspatial (very high spatial resolution) imagery is well-suited for detecting small-scale changes to landscapes that may portend future larger-scale changes. Early identification of these small-scale changes may be key to the success of efforts that seek to mitigate land-use and land-cover change trends.

The hyperspatial imagery produced by Unmanned Autonomous Systems (UAS, aka drones) and associated data processing methods have recently been used in a variety of applications. Their use in land-use and land-cover mapping and in landscape change analysis allow for monitoring of small-scale, potentially rapid, changes like the health of and disease occurrence in individual plant species. In forestry applications this means that hyperspatial UAS imagery may enable the detection of individual trees or clusters of identical tree types based on characteristics invisible with coarser resolution imagery. One important tree characteristic that only becomes possible to measure with hyperspatial imagery is the tree canopy texture, or the pixel-to-pixel variation of intensity caused by

the physical structure of the tree canopy (e.g., its height, shape, the orientation of its leaves, branches, their shadows, etc.).

This study sought to build a methodological framework for detecting species level differences by creating and analyzing tree canopy texture derived from drone-based hyperspatial data. The goal was to answer the following questions:

1. Are texture patterns derived from hyperspatial digital surface models (DSM) of the tree canopy indicators of individual tree species?
2. What is the role of texture in determining species-level assemblages and individual tree entities?
3. Can texture alone match reflectance-based LULC detection methods in accuracy of classification?

Tree canopy texture was captured in this research by applying Structure from Motion (SfM) techniques to overlapping UAS photographs to create a hyperspatial resolution RGB image mosaic and digital surface model (DSM). The Gray Level Co-occurrence Matrix (GLCM) was used to calculate the tree canopy texture from the DSM, and the RGB image mosaic and the tree canopy texture were used in combination to test the effectiveness of canopy texture on tree classification in a Texas Hill Country environment.

Image segmentation was first used to delineate the forested area at the study site and then three techniques were used to classify tree species. The three techniques were (1) Geographic Object-based Image Analysis (GEOBIA) (i.e., image segmentation, object attribution and object classification) using UAS-based hyperspatial RGB imagery

with the corresponding GLCM measure of tree canopy texture, (2) pixel-based, supervised maximum likelihood classification using the UAS-based hyperspatial imagery, and (3) GEOBIA using commonly available National Agricultural Imagery Product (NAIP) imagery and a measure of NDVI derived from the NAIP imagery.

Findings indicated that the use of GEOBIA techniques with UAS-based RGB imagery and a GLCM-based measure of tree canopy yielded an 81.18% overall accuracy with a Z score of 10 indicating these results were significantly better than random (Table 3). The UAS-based RGB imagery classified without texture and using a pixel-based Maximum Likelihood classifier yielded an overall accuracy of 78.24%, and the NAIP-based VNIR/NDVI imagery classified with GEOBIA techniques yielded an overall accuracy of 75.29%. This study has shown the texture-based method to be as good as the other measures when considered at the 95% confidence level. The tests resulted in a confidence level of 0.81 for the DSM vs. NDVI test and 0.49 for DSM vs. maximum likelihood with an improvement in overall accuracy for both tests. The conclusion is that the texture patterns derived from the tree canopy DSM are indicators of individual tree species and can match the reflectance-only based methods in accuracy.

To answer the question of what role texture plays in the determination of tree assemblages one must directly compare the DSM texture patterns to the physical structure of the tree species being studied. Visually, texture is the pattern of variations in contrast of the colors of an object. If one were to start with the texture model and work backwards to the original imagery and then directly observe the object in the imagery one could see where the dark areas, in general, correspond to openings in the canopy, or areas with depth, and lighter areas would be the highest parts of the canopy. Expanding on

these observations, if one were to observe a mix of highly contrasting pixels in one area it is likely this is an area of low leaf density where there are high and low elevation areas within close proximity of each other. Subsequently a low contrast area, an area with variation of grey pixels, would likely correspond to moderate leaf density or perhaps an area of high density with small leaves. These patterns which are processed and grouped with the GEOBIA software are now directly relatable to specific types of canopy structure.

The results of this study indicate that, while not statistically significantly better, the DSM, texture-based method is at least as good as the traditional reflectance-based methods. Table 4 shows a better overall accuracy for the DSM, texture-based method and significant results for all three methods when compared to random. Table 5 shows the results of the comparisons of the DSM-based texture method vs. the reflective-bands method at the confidence level of 0.81, and for the comparison of the DSM-based texture method vs. the NDVI maximum likelihood method at the confidence level of 0.49.

Ecosystem disturbances are something that will always be present in our environment. Whether man-made or natural these disturbances can have long-lasting impacts. By demonstrating that hyperspatial, object-based analysis and mapping can yield acceptable results in comparison with traditional methods, I believe I have opened a pathway to further exploration of these techniques. These methods dig deeper into what was happening at the time the data were gathered and can be analyzed near-real time rather than showing the result of what took place as you would see when examining historic datasets.

By demonstrating in this study that techniques utilizing texture and GEOBIA can equal the results of traditional remote sensing methods I believe that more new studies should not limit themselves to the pixel. As new technology developed for remote sensing starts to penetrate all aspects of human life as other technologies have done in the past, we need to look beyond what has been and start looking at what can be. The technology is here now that allows analysis beyond the pixel and on to statistical analysis of the patterns these pixels build up.

Study Limitations

The analysis in this study is limited to data acquired on a single day at a single location. Therefore, any variability due to changes in conditions from weather, canopy density, flight conditions, or annual phenological stage are not considered. Since completion of the data processing of this study, the author has had opportunities to use several alternate SfM software packages and has found great variability in the quality of the output generated. It has also been discovered that the locations of ground control points relative to each other can influence the quality of the output. When considering all these possible variations one can conclude that this study is just a very narrow band within a full spectrum of possibilities for UAS-based, DSM-based GEOBIA classification studies.

Future research should consider a testing of accuracy of these various software packages and the effect of ground control positioning on final results. Future work should also include a sensor capable of recording NIR so the NDVI data can be gathered with

the drone. It would be valuable to know if the additional resolution would produce significantly more accurate NDVI results.

This study was additionally limited by the maximum resolution of NAIP imagery. Under ideal circumstances both data sets (UAS imagery and NAIP imagery) would have been of similar resolution to eliminate the possibility that the difference in resolution would have an effect on the outcome. At this time NAIP imagery of this quality is not available. It would be possible to equip a drone with a CIR/RGB sensor to create NDVI data at a similar resolution to the texture data.

Future Work

As drone, camera and software capabilities continue to improve it will be worthwhile to explore the texture-based classification methodology again. Considering this methodology proved to be as good as existing methods, it may show improvements as the technologies involved mature.

For the near future this study shows that those interested in texture-based classification should not exclusively rely on texture. Future researchers should consider utilizing additional ancillary data sources to enhance the texture classifications. These data sources can include spectral data in both the visible and non-visible spectrums, leaf area indexes (LAI), canopy volume calculations and many other types of remotely sensed data. Future studies relying exclusively on texture may also wish to gather data during different stages of the phenological cycle and implement change detection into the classification routine.

This study has also proven that accurate land cover surveys can be accomplished using relatively inexpensive unmanned systems. While NAIP imagery is available for free this data is often months or even years old. When there is a need for fresh data, unmanned systems are now a very viable alternative to expensive manned flights.

Land cover analysis using drones is in its infancy and is progressing rapidly. More studies involving SfM land cover studies are essential. This study was successful at matching current measures so it should be given further study when considering how early this technology is in development.

It would be prudent to review the methodology to see if there are any potential areas where changes could improve the results. One factor worth considering is weather conditions on data gathering days. In this study every effort was made to fly at times that had the best possible conditions. Unfortunately, it was not possible to wait for optimum weather conditions and flying had to be conducted within a certain timeframe. Ideally, wind speed would be near zero to obtain the absolute best canopy DSM but that was not the case on the days flying was conducted. Winds were generally light between 8-13 kph but there was still some canopy movement detectable in the imagery mosaics. The degree to which wind affected the final results is unknown, but it merits further consideration.

Drone technology is advancing rapidly and also decreasing in cost. The FAA has now relaxed restrictions on commercial and educational drone operations allowing for data gathering where it was previously illegal without specific clearance from the FAA for a given property.

While not part of the primary research questions, some data relative to the costs and ease of use of each model were noted and may be of use to future researchers. The least expensive of the three is the NDVI model utilizing the NAIP imagery. The imagery is free to download so the only cost is the software and the time to process and analyze. ESRI's ArcMap, with the proper extensions, as well as ERDAS Imagine, is capable of NDVI analysis. University GIS departments will likely already have ArcMap as do many private companies involved in cartography or environmental studies which would essentially negate that cost as it has already been acquired. There are also free online tools for NDVI analysis such as Drone Data Management System (DDMS). DDMS requires only an account registration after which one may upload and process imagery with a variety of tools. However, the free account limits the resolution of the output. There is a paid account which allows higher resolution output. These free tools will not be as robust as the ESRI and ERDAS software but do offer a no/low-cost alternative if that software is not available.

The UAS-based maximum likelihood model falls in the middle of the three in terms of cost. Software for analysis is essentially the same as the NDVI model. The additional cost is the drone equipment, processing software and time to process the imagery to a point where it is in the same state as the downloadable NAIP imagery.

Currently, the UAS-based GEOBIA model is the costliest of the three. This will likely change as will be explained. This model requires everything the two models above utilize with the addition of software for the object-based analysis. The change referred to is that as of version 10.3 ESRI has begun including GEOBIA tools as part of their Spatial

Analyst extension. The functionality is not as robust as Trimble eCognition but that will likely change in the coming software upgrades. If ESRI begins to include tools that match the capability of eCognition it will make the costs of the two drone-based methods equal.

While the two drone-based models are the most expensive to implement they have one distinct advantage—the advantage of data acquisition when desired. With NAIP imagery one is limited to, at best, new data once a year. With the drone-based models, data acquisition can happen anytime weather permits. This advantage alone can make the added cost of the drone-based models desirable.

APPENDIX

AERIAL PHOTOGRAPHY PLATFORMS

The rotorcraft is a model X8 built by 3D Robotics (Figure 12). It is classified as an octaquad as it utilizes eight motors and propellers on four arms. Specifications for the system are listed below.

- Battery: 4S 14.8V 10,000 mAh 10C
- Battery Dimensions: 6.6 in x 2.6 in x 1.4 in (16.7 cm x 6.5 cm x 3.5 cm)
- Battery Weight: 803 g
- Autopilot hardware: Pixhawk v2.4.5
- Autopilot firmware: ArduCopter 3.2
- GPS: 3DR u-blox GPS with Compass (LEA-6H module, 5 Hz update)
- Ground Station Radio: 3DR Radio v2 (915 MHz)
- Motors: SunnySky V2216-12 KV800 II Controller: FlySky FS-TH9X with FrSky telemetry module
- Frame Type: X
- Propellers: APC Propeller 11x4.7 SF (4), APC Propeller 11x4.7 SFP (4)
- Vehicle Dimensions: 13.7 in x 20.1 in x 11.8 in (35 cm x 51 cm x 20 cm)
- Payload Capacity: 800 g (1.7 lbs). Vehicle Weight with Battery: 2.56 kg (5.6 lbs)
- Maximum Estimated Flight Time: 15 min

The camera is a Gopro 3+ Black$^{(TM)}$ capable of shooting 12 megapixel still photos in a wide angle fisheye format. The camera is mounted on a 2D gimble for stability.

The X8 is launched from the ground by manual controls until it reaches an altitude of about 10 meters above ground level (AGL). Once the X8 has reached that altitude it is switched to autopilot mode and it begins to fly its pre-programmed mission. The X8 is monitored at all times via a wireless link to a ground station which tracks and stores the telemetry. The flight plan typically ranges between 30 and 50 meters AGL, speed during photography is approximately 5 meters per second and the camera fires one time per second which is programmed directly into the camera rather than controlled by the computer or autopilot. Because of the preprogrammed timing of the photographs it is not

possible to detect regions of little image overlap, that may result from drift or increased speed due to tailwinds, until after the X8 has landed and data has been downloaded and processed. The values for optimal speed and altitude are based on more than two years of test flights at the study area. These flights were conducted at varying altitudes, and speeds to determine what parameters yielded the sharpest images. A typical flight can yield between 300 and 600 individual photos depending on flight time. Upon completing the programmed flight, the X8 will return to the launch point automatically and hover at a predetermined altitude. At this point the operator takes manual control for landing.

Figure 12 - 3D Robotics X8 Rotorcraft Drone

The fixed wing platform is the AreoHawk manufactured in New Zealand by Hawkeye UAV (Figure 8). This is a large survey grade system and requires a minimum of two people to operate. AreoHawk specifications are listed below.

- Dimensions 5.1 – 5.8 kg 2.65m wingspan 1.47m
- 120 min + endurance Electric motor
- Cruise speed 60-70 km/hr
- Service ceiling 4,300 meters
- Max 45 km/hr wind capability
- 900 MHz spread-spectrum frequency hopping
- 30 Km range Multiple control station operation

The camera utilized with the Areohawk is a Sony Nex7$^{(TM)}$ with a wide angle survey lens. The Nex7$^{(TM)}$ is a high-end mirrorless digital camera in a small form factor allowing it to fit into a small space (due to size of the limited space in the airframe) but still having the capabilities of a full sized SLR. The Nex7 has a full-size, 24.3-megapixel APS-C sensor.

The AreoHawk is hand-launched by one individual while a second person monitors the systems on the ground station. The takeoff after launch is autonomous but the ground station is capable of taking over at any time in case of any malfunctions. Once in the air the AreoHawk automatically goes into loiter mode until it is instructed to begin the photography mission. Once the mission commences it can fly a preprogrammed pattern or it can be maneuvered through point and clicks on the ground station computer screen. Each time a photograph is taken the footprint is overlaid on the ground station screen. This eliminates most problems with missed areas because the operator can see the image footprints in real-time on the computer screen and either alter the flight parameters or manually re-shoot missed areas.

Figure 13 - Hawkeye AreoHawk Survey Grade Fixed Wing UAS

Upon completing the photography mission, the AreoHawk returns to the launch point and at a predetermined altitude will deploy a recovery parachute. The parachute deployment point is automatically determined based upon the desired landing zone, wind speed, and direction.

REFERENCES

Agarwal, S., L. S. Vailshery, M. Jaganmohan, and H. Nagendra. 2013. Mapping Urban Tree Species Using Very High Resolution Satellite Imagery: Comparing Pixel-Based and Object-Based Approaches. *ISPRS International Journal of Geo-Information* 2 (1):220–236. https://www.mdpi.com/2220-9964/2/1/220/htm (last accessed 18 October 2021).

Akar, O., and E. T. Gormus. 2021. Land use/land cover mapping from airborne hyperspectral images with machine learning algorithms and contextual information. *Geocarto International* 36 (1):21–26. https://www.tandfonline.com/doi/abs/10.1080/10106049.2021.1945149 (last accessed 18 October 2021).

Asner, G. P., and K. B. Heidebrecht. 2010. Spectral unmixing of vegetation, soil and dry carbon cover in arid regions: Comparing multispectral and hyperspectral observations. *International Journal of Remote Sensing* 23 (19):3939–3958. https://www.tandfonline.com/doi/abs/10.1080/01431160110115960 (last accessed 18 October 2021).

Baccus, J. T., H. M. Becker, T. R. Simpson, and R. W. Manning. 2000. *Mammals of the Freeman Ranch*. San Marcos, Tx.

Bai, Y., G. Sun, Y. Li, P. Ma, G. Li, and Y. Zhang. 2021. Comprehensively analyzing optical and polarimetric SAR features for land-use/land-cover classification and urban vegetation extraction in highly-dense urban area. *International Journal of Applied Earth Observation and Geoinformation* 103:102–112.

Black, M., P. Carbonneau, M. Church, and J. Warburton. 2014. Mapping sub-pixel fluvial grain sizes with hyperspatial imagery. *Sedimentology* 61 (3):691–711. https://onlinelibrary.wiley.com/doi/full/10.1111/sed.12072 (last accessed 18 October 2021).

Blaschke, T. 2010. Object based image analysis for remote sensing. *ISPRS Journal of Photogrammetry and Remote Sensing* 65 (1):2–16.

Boyd, D. S., and F. M. Danson. 2005. Satellite remote sensing of forest resources: three decades of research development. *Progress in Physical Geography* 29 (1):1–26.

Caballero, G. R., G. Platzeck, A. Pezzola, A. Casella, C. Winschel, S. S. Silva, E. Ludueña, N. Pasqualotto, and J. Delegido. 2020. Assessment of Multi-Date Sentinel-1 Polarizations and GLCM Texture Features Capacity for Onion and Sunflower Classification in an Irrigated Valley: An Object Level Approach. *Agronomy* 10 (6). https://www.mdpi.com/2073-4395/10/6/845.

Castillejo-González, I. L., F. López-Granados, A. García-Ferrer, J. M. Peña-Barragán, M. Jurado-Expósito, M. S. de la Orden, and M. González-Audicana. 2009. Object- and pixel-based analysis for mapping crops and their agro-environmental associated measures using QuickBird imagery. *Computers and Electronics in Agriculture* 68 (2):207–215.

Congalton, R. 2004. Putting the Map Back in Map Accuracy Assessment. In *Remote Sensing and GIS Accuracy Assessment*, 1–11. Boca Raton, Fl: CRC Press.

Congalton, R., and K. Green. 2019. *Assessing the Accuracy of Remotely Sensed Data: Principles and Practices* 3rd ed. Boca Raton, Fl: CRC Press.

Crafts, N. F. R. 1996. The First Industrial Revolution: A Guided Tour for Growth Economists. *American Economic Review* 86 (2):197–201.

Culbert, P. D., V. C. Radeloff, V. St-Louis, C. H. Flather, C. D. Rittenhouse, T. P. Albright, and A. M. Pidgeon. 2012. Modeling broad-scale patterns of avian species richness across the Midwestern United States with measures of satellite image texture. *Remote Sensing of Environment* 118:140–150.

Cunliffe, A. M., R. E. Brazier, and K. Anderson. 2016. Ultra-fine grain landscape-scale quantification of dryland vegetation structure with drone-acquired structure-from-motion photogrammetry. *Remote Sensing of Environment* 183:129–143. https://linkinghub.elsevier.com/retrieve/pii/S0034425716302206 (last accessed 18 October 2021).

Deane, P. M. 1980. *The First Industrial Revolution* 2nd ed. Cambridge: Cambridge University Press. https://www.cambridge.org/core/books/first-industrial-revolution/56BCD4D8F433A55735432B24E851CE22.

Deliry, S. I., and U. Avdan. 2021. Accuracy of Unmanned Aerial Systems Photogrammetry and Structure from Motion in Surveying and Mapping: A Review. *Journal of the Indian Society of Remote Sensing* 49.

Dingle Robertson, L., and D. King. 2011. Comparison of pixel- and object-based classification in land cover change mapping. *International Journal of Remote Sensing* 32:1505–1529.

Dong, P., and Q. Chen. 2017. *LiDAR Remote Sensing and Applications* 1st ed. Boca Raton, Fl: CRC Press.

Drummond, M. A., and R. Auch. 2016. Land Cover Trends In U.S. Geological Survey. http://landcovertrends.usgs.gov/gp/regionalSummary.html (last accessed 9 February 2022).

Earl, R. A., R. W. Dixon, and C. A. Day. 2006. Long Term Precipitation and Water Supply Variability in South-Central Texas. In *Proceedings and Papers of the Applied Geography Conferences*, 29:11–22.

European Space Agency (ESA). 2013. European S. A. Earthnet Online: Texture and Image Analysis. In European Space Agency. http://earth.esa.int/applications/data_util/SARDOCS/spaceborne/Radar_Courses/Radar_Course_III/texture.htm (last accessed 10 February 2013).

Fonseca, L. M. G., T. S. Körting, H. do N. Bendini, C. D. Girolamo-Neto, A. K. Neves, A. R. Soares, E. C. Taquary, and R. V. Maretto. 2021. Pattern Recognition and Remote Sensing techniques applied to Land Use and Land Cover mapping in the Brazilian Savannah. *Pattern Recognition Letters* 148:54–60.

Foody, G. M. 2002. Status of land cover classification accuracy assessment. *Remote Sensing of Environment* 80 (1):185–201.

Foody, G. M. 2009. Sample size determination for image classification accuracy assessment and comparison. *International Journal of Remote Sensing* 30 (20):5273–5291. https://www.tandfonline.com/doi/abs/10.1080/01431160903130937 (last accessed 18 October 2021).

Franklin, S. E., R. J. Hall, L. M. Moskal, a. J. Maudie, and M. B. Lavigne. 2000. Incorporating texture into classification of forest species composition from airborne multispectral images. *International Journal of Remote Sensing* 21 (1):61–79.

Froidevaux, J. S. P., F. Zellweger, K. Bollmann, G. Jones, and M. K. Obrist. 2016. From field surveys to LiDAR: Shining a light on how bats respond to forest structure. *Remote Sensing of Environment* 175:242–250.

Gao, Y., and J. Mas. 2008. A comparison of the performance of pixel based and object based classifications over images with various spatial resolutions. *Online Journal of Earth Science* 2:27–35.

Geist, H. J., and E. F. Lambin. 2002. Proximate Causes and Underlying Driving Forces of Tropical Deforestation: Tropical forests are disappearing as the result of many pressures, both local and regional, acting in various combinations in different geographical locations. *BioScience* 52 (2):143–150. https://doi.org/10.1641/0006-3568(2002)052[0143:PCAUDF]2.0.CO (last accessed 18 October 2021).

Greenberg, J. A., S. Z. Dobrowski, and V. C. Vanderbilt. 2009. Limitations on maximum tree density using hyperspatial remote sensing and environmental gradient analysis. *Remote Sensing of Environment* 113 (1):94–101.

Groom, M., G. Meffe, and C. Carroll. 2006. *Principles of Conservation Biology*. Sunderland, MA.: Sinauer Associates.

Hall-Beyer, M. 2017. *GLCM Texture: A Tutorial v. 3.0*. Calgary. https://www.researchgate.net/publication/315776784_GLCM_Texture_A_Tutorial_v_30_March_2017 (last accessed 4 March 2021).

Husson, E., F. Ecke, and H. Reese. 2016. Comparison of Manual Mapping and Automated Object-Based Image Analysis of Non-Submerged Aquatic Vegetation from Very-High-Resolution UAS Images. *Remote Sensing* 8 (9):1202–1224. https://www.mdpi.com/2072-4292/8/9/724 (last accessed 5 April 2021).

Iqbal, N., R. Mumtaz, U. Shafi, and S. M. H. Zaidi. 2021. Gray level co-occurrence matrix (GLCM) texture based crop classification using low altitude remote sensing platforms. *Computer Science* 7:536–537. https://pubmed.ncbi.nlm.nih.gov/34141878 (last accessed 3 February 2021).

Jeffrey Lovich. 2022. Saltcedar. https://cisr.ucr.edu/invasive-species/saltcedar.

Jensen, J. R. 1986. *Introductory Digital Image Processing: A Remote Sensing Perspective* 1st ed. Hoboken, NJ: Prentice-Hall.

Kavzoglu, T., and M. Yildiz. 2014. Parameter-Based Performance Analysis of Object-Based Image Analysis Using Aerial and Quikbird-2 Images. *ISPRS Annals of the Photogrammetry, Remote Sensing and Spatial Information Sciences* II–7:31–37. https://doi.org/10.5194%2Fisprsannals-ii-7-31-2014 (last accessed 24 January 2022).

Kerr, J. T., and M. Ostrovsky. 2003. From space to species: ecological applications for remote sensing. *Trends in Ecology & Evolution* 18 (6):299–305.

Kupidura, P. 2019. The Comparison of Different Methods of Texture Analysis for Their Efficacy for Land Use Classification in Satellite Imagery. *Remote Sensing* 11 (10). https://www.mdpi.com/2072-4292/11/10/1233.

Lambin, E. F., and P. Meyfroidt. 2011. Global land use change, economic globalization, and the looming land scarcity. *Proceedings of the National Academy of Sciences* 108 (9):3465–3472. https://www.pnas.org/content/108/9/3465 (last accessed 3 February 2021).

Lambin, E. F., B. Turner II, H. J. Geist, B. Agbola, A. Angelsen, J. W. Bruce, O. Coomes, R. Dirzo, G. Fischer, C. Folke, P. S. George, K. Homewood, J. Imbernon, R. Leemans, X. Li, E. Moran, M. Mortimore, P. S. Ramakrishnan, J. F. Richards, and J. Xu. 2001. The causes of land-use and land-cover change: Moving beyond the myths. *Global Environmental Change-Human and Policy Dimensions* 11 (4):261–269.

Lambin, E., and H. Geist. 2006. *Land-Use and Land-Cover Change: Local Processes and Global Impacts* 1st ed. Berlin, Heidelberg: Springer.

Lambin, E., H. Geist, and E. Lepers. 2003. Dynamics of Land-use and land-cover change in tropical regions. *Annual Review of Environment and Resources* 20:49205–49241.

de Leeuw, W., P. Verschure, and R. van Liere. 2006. Visualization and Analysis of Large Data Collections: a Case Study Applied to Confocal Microscopy Data. *IEEE Transactions on Visualization and Computer Graphics* 12 (5):1251–1258.

Liao, J., J. Zhou, and W. Yang. 2021. Comparing LiDAR and SfM digital surface models for three land cover types. *Open Geosciences* 13 (1):497–504. https://doi.org/10.1515/geo-2020-0257.

Lillesand, T., R. Kiefer, and J. Chipman. 2004. *Remote Sensing and Image Interpretation (Fifth Edition)*. Hoboken, NJ: Wiley.

Liu, Y., Y. Hu, and L. Peng. 2005. Accurate Quantification of Grassland Cover Density in an Alpine Meadow Soil Based on Remote Sensing and GPS. *Pedosphere* 15 (6):778–783.

Lo, C. P., and L. J. Watson. 1998. The Influence of Geographic Sampling Methods on Vegetation Map Accuracy Evaluation in a Swampy Environment. *Photogrammetric Engineering and Remote Sensing* 64:1189–1200.

Loveland, T. R., and W. Acevedo. 2016. Land Cover Change. *Land Cover Trends*. http://landcovertrends.usgs.gov/east/regionalSummary.html (last accessed 21 October 2021).

Ludeke, K., D. German, and J. Scott. 2007. *Texas Vegetation Classification Project: Interpretive Booklet for Phase I*. Austin. https://morap.missouri.edu/wp-content/uploads/2019/02/Texas_Vegetation_Classification_Phase_1_Interpretive_Booklet.pdf (last accessed 18 February 2022).

Luus, K. A., D. T. Robinson, and P. J. Deadman. 2013. Representing ecological processes in agent-based models of land use and cover change. *Journal of Land Use Science* 8 (2):175–198. https://doi.org/10.1080/1747423X.2011.640357 (last accessed 7 December 2021).

Mallet, C., and F. Bretar. 2009. Full-waveform topographic lidar: State-of-the-art. *ISPRS Journal of Photogrammetry and Remote Sensing* 64 (1):1–16. https://www.sciencedirect.com/science/article/pii/S0924271608000993 (last accessed 3 February 2021).

Mansor, S., W. T. Hong, and A. R. M. Shariff. 2002. Object oriented classification for land cover mapping. In *Proceedings of the 23rd Asian Conference on Remote Sensing*, 25–29. Taipei, Taiwan.

Martínez Sánchez, J., Á. Váquez Álvarez, D. López Vilariño, F. Fernández Rivera, J. C. Cabaleiro Domínguez, and T. Fernández Pena. 2019. Fast Ground Filtering of Airborne LiDAR Data Based on Iterative Scan-Line Spline Interpolation. *Remote Sensing* 11 (19). https://www.mdpi.com/2072-4292/11/19/2256 (last accessed 6 May 2021).

McCarley, T. R., C. A. Kolden, N. M. Vaillant, A. T. Hudak, A. M. S. Smith, B. M. Wing, B. S. Kellogg, and J. Kreitler. 2017. Multi-temporal LiDAR and Landsat quantification of fire-induced changes to forest structure. *Remote Sensing of Environment* 191:419–432. https://www.sciencedirect.com/science/article/pii/S0034425716305016 (last accessed 1 February 2021).

Meng, X., N. Currit, and K. Zhao. 2010. Ground Filtering Algorithms for Airborne LiDAR Data: A Review of Critical Issues. *Remote Sensing* 2 (3):833–860. https://www.mdpi.com/2072-4292/2/3/833.

Meyer, W. B., and B. L. Turner II. 1992. Human Population Growth and Global Land-Use/Cover Change. *Annual Review of Ecology and Systematics* 23 (1):39–61. https://doi.org/10.1146/annurev.es.23.110192.000351 (last accessed 24 January 2022).

Mlambo, R., I. H. Woodhouse, F. Gerard, and K. Anderson. 2017. Structure from Motion (SfM) Photogrammetry with Drone Data: A Low Cost Method for Monitoring Greenhouse Gas Emissions from Forests in Developing Countries. *Forests* 8 (3). https://www.mdpi.com/1999-4907/8/3/68 (last accessed 5 May 2021).

Moskal, L., and S. Franklin. 2004. Relationship between airborne multispectral image texture and aspen defoliation. *International Journal of Remote Sensing* 25:2701–2711.

Murphy, R., A. J. Underwood, T. Tolhurst, and M. G. Chapman. 2008. Field-based remote-sensing for experimental intertidal ecology: Case studies using hyperspatial and hyperspectral data for New South Wales (Australia). *Remote Sensing of Environment* 112:3353–3365.

Myint, S. W., P. Gober, A. Brazel, S. Grossman-Clarke, and Q. Weng. 2011. Per-pixel vs. object-based classification of urban land cover extraction using high spatial resolution imagery. *Remote Sensing of Environment* 115 (5):1145–1161. https://www.sciencedirect.com/science/article/pii/S0034425711000034 (last accessed 1 February 2021).

Ngo, K. D., K. D. Ngo, A. M. Lechner, and T. T. Vu. 2020. Land cover mapping of the Mekong Delta to support natural resource management with multi-temporal Sentinel-1A synthetic aperture radar imagery. *Remote sensing applications* 17:272–275. https://dx.doi.org/10.1016/j.rsase.2019.100272 (last accessed 24 January 2022).

Niemeyer, I., and M. Canty. 2003. Pixel-based and object-oriented change detection analysis using high-resolution imagery. In *Proceedings 25th Symposium on Safeguards and Nuclear Material Management*, 2133–2136. Stockholm, Sweden.

Norman, J. M., and G. S. Campbell. 1989. Canopy structure. In *Plant Physiological Ecology: Field methods and instrumentation*, eds. R. W. Pearcy, J. R. Ehleringer, H. A. Mooney, and P. W. Rundel, 301–325. Dordrecht: Springer Netherlands https://doi.org/10.1007/978-94-009-2221-1_14 (last accessed 24 January 2022).

Numbisi, F. N., F. M. B. Van Coillie, and R. De Wulf. 2019. Delineation of Cocoa Agroforests Using Multiseason Sentinel-1 SAR Images: A Low Grey Level Range Reduces Uncertainties in GLCM Texture-Based Mapping. *ISPRS International Journal of Geo-Information* 8 (4). https://www.mdpi.com/2220-9964/8/4/179.

Olofsson, P., G. M. Foody, M. Herold, S. V Stehman, C. E. Woodcock, and M. A. Wulder. 2014. Good practices for estimating area and assessing accuracy of land change. *Remote Sensing of Environment* 148:42–57. https://www.sciencedirect.com/science/article/pii/S0034425714000704 (last accessed 3 October 2021).

Oruc, M., A. Marangoz, and G. Buyuksalih. 2004. Comparison of Pixel-Based and Object-Oriented Classification Approaches Using Landsat-7 ETM Spectral Bands. In *Proceedings of International Archives of Photogrammetry & Remote Sensing*, 1118–1123. Indianapolis, In.

Ramola, A., A. Shakya, and D. Pham. 2020. Study of statistical methods for texture analysis and their modern evolutions. *Engineering Reports* 2 (4):1–24.

Rampun, A., H. Strange, and R. Zwiggelaar. 2013. Texture Segmentation Using Different Orientations of GLCM Features. In *6th International Conference on Computer Vision / Computer Graphics*. Shanghai, China.

Rocchini, D., G. M. Foody, H. Nagendra, C. Ricotta, M. Anand, K. S. He, V. Amici, B. Kleinschmit, M. Förster, S. Schmidtlein, H. Feilhauer, A. Ghisla, M. Metz, and M. Neteler. 2013. Uncertainty in ecosystem mapping by remote sensing. *Computers & Geosciences* 50:128–135.

Salas, E., K. Boykin, and R. Valdez. 2016. Multispectral and Texture Feature Application in Image-Object Analysis of Summer Vegetation in Eastern Tajikistan Pamirs. *Remote Sensing* 8:78–101.

Smith, M., J. Carrivick, and D. Quincey. 2015. Structure from Motion Photogrammetry in Physical Geography. *Progress in Physical Geography* 40 (2):247–275.

Snedecor, G., and W. Cochran. 1967. *Statistical Methods* 6th ed. Ames, Iowa: Iowa State University Press.

Soulard, C. E., and B. M. Sleeter. 2012. Late twentieth century land-cover change in the basin and range ecoregions of the United States. *Regional Environmental Change* 12:813–823.

Strecha, C., A. Fletcher, A. Lechner, P. Erskine, and P. Fua. 2012. Developing Species Specific Vegetation Maps Using Multi-spectral Hyperspatial Imagery from Unmanned Aerial Vehicles. In *ISPRS Annals of Photogrammetry, Remote Sensing and Spatial Information Sciences*, 311–316. Melbourne, Australia: Copernicus Publications.

Tamminga, A., C. Hugenholtz, B. Eaton, and M. Lapointe. 2015. Hyperspatial Remote Sensing of Channel Reach Morphology and Hydraulic Fish Habitat Using an Unmanned Aerial Vehicle (UAV): A First Assessment in the Context of River Research and Management. *River Research and Applications* 31 (3):379–391. https://doi.org/10.1002/rra.2743 (last accessed 24 January 2022).

Tareen, S. A. K., and Z. Saleem. 2018. A comparative analysis of SIFT, SURF, KAZE, AKAZE, ORB, and BRISK. In *2018 International Conference on Computing, Mathematics and Engineering Technologies (iCoMET)*, 1–10. Sukkur, Pakistan.

Tassi, A., and M. Vizzari. 2020. Object-Oriented LULC Classification in Google Earth Engine Combining SNIC, GLCM, and Machine Learning Algorithms. *Remote Sensing* 12 (22). https://www.mdpi.com/2072-4292/12/22/3776.

Tavus, B., S. Kocaman, and C. Gokceoglu. 2022. Flood damage assessment with Sentinel-1 and Sentinel-2 data after Sardoba dam break with GLCM features and Random Forest method. *Science of The Total Environment* 816:151585. https://www.sciencedirect.com/science/article/pii/S0048969721066638.

Texas Parks and Wildlife. 2021. Ecological Mapping Systems. https://tpwd.texas.gov/landwater/land/programs/landscape-ecology/ems/ (last accessed 10 February 2022).

Thakare, S., R. P. Arbal, and M. Shahade. 2011. Artificial Intelligence with Stereo Vision Algorithms and its Methods. In *International Conference on Recent Trends in Information Technology and Computer Science*, 1–5. Chennai, India.

Turner, W., S. Spector, N. Gardiner, M. Fladeland, E. Sterling, and M. Steininger. 2003. Remote sensing for biodiversity science and conservation. *Trends in Ecology & Evolution* 18 (6):306–314.

Tuttle, E. M., R. R. Jensen, V. A. Formica, and R. A. Gonser. 2006. Using Remote Sensing Image Texture to Study Habitat Use Patterns: A Case Study Using the Polymorphic White-Throated Sparrow (Zonotrichia albicollis). *Global Ecology and Biogeography* 15 (4):349–357. http://www.jstor.org/stable/3697538 (last accessed 3 October 2021).

U.S. Climate Data Center. 2021. Climate Texas - Average Rainfall and Temperature. https://www.usclimatedata.com/climate/texas/united-states/3213 (last accessed 11 February 2022).

Ulaby, F. T., F. Kouyate, B. Brisco, and T. H. L. Williams. 1986. Textural Infornation in SAR Images. *IEEE Transactions on Geoscience and Remote Sensing* 24 (2):235–245.

Walker, B., D. Salt, and W. Reid. 2006. *Resilience Thinking: Sustaining Ecosystems and People in A Changing World* 1st ed. Washington D.C.: Island Press.

Wallace, L., A. Lucieer, Z. Malenovský, D. Turner, and P. Vopěnka. 2016. Assessment of Forest Structure Using Two UAV Techniques: A Comparison of Airborne Laser Scanning and Structure from Motion (SfM) Point Clouds. *Forests* 7 (3):62–66. https://www.mdpi.com/1999-4907/7/3/62.

Weigand, M., J. Staab, M. Wurm, and H. Taubenböck. 2020. Spatial and semantic effects of LUCAS samples on fully automated land use/land cover classification in high-resolution Sentinel-2 data. *International Journal of Applied Earth Observation and Geoinformation* 88:567–598. https://www.sciencedirect.com/science/article/pii/S0303243419307317 (last accessed 22 January 2022).

Westoby, M. J., J. Brasington, N. F. Glasser, M. J. Hambrey, and J. M. Reynolds. 2012. 'Structure-from-Motion' photogrammetry: A low-cost, effective tool for geoscience applications. *Geomorphology* 179:300–314. https://www.sciencedirect.com/science/article/pii/S0169555X12004217 (last accessed 22 January 2022).

Whiteside, T. G., G. S. Boggs, and S. W. Maier. 2011. Comparing object-based and pixel-based classifications for mapping savannas. *International Journal of Applied Earth Observation and Geoinformation* 13 (6):884–893. https://www.sciencedirect.com/science/article/pii/S0303243411000912 (last accessed 22 January 2022).

Wiggins, H., C. Nelson, A. Larson, and H. Stafford. 2019. Using LiDAR to develop high-resolution reference models of forest structure and spatial pattern. *Forest Ecology and Management* 434:318–330.

Willhauck, G. 2000. Comparison of object oriented classification techniques and standard image analysis for the use of change detection between SPOT multispectral satellite images and aerial photos. In *International Archives of Photogrammetry and Remote Sensing*, 11–22.

Wilson, E. O. 1988. *Biodiversity*. Washington DC: The National Academies Press .

Wu, Q., R. Zhong, W. Zhao, K. Song, and L. Du. 2019. Land-cover classification using GF-2 images and airborne lidar data based on Random Forest. *International Journal of Remote Sensing* 40 (5–6):2410–2426. https://doi.org/10.1080/01431161.2018.1483090.

Xiao, J., Y. Shen, J. Ge, R. Tateishi, C. Tang, Y. Liang, and Z. Huang. 2006. Evaluating urban expansion and land use change in Shijiazhuang, China, by using GIS and remote sensing. *Landscape and Urban Planning* 75 (1):69–80. https://www.sciencedirect.com/science/article/pii/S0169204605000058.

Yacouba, D., X. Wen, Y. Diallo, and G. Hu. 2009. Applications of Remote Sensing in Land Use/Land Cover Change Detection in Puer and Simao Counties, Yunnan Province. *Journal of American Science* 5 (4):157–166. http://www.americanscience.org (last accessed 18 October 2021).

Yu, H., W. Yang, G.-S. Xia, and G. Liu. 2016. A Color-Texture-Structure Descriptor for High-Resolution Satellite Image Classification. *Remote Sensing* 8:259–275.

Zhang, R., and D. Zhu. 2011. Study of land cover classification based on knowledge rules using high-resolution remote sensing images. *Expert Systems with Applications* 38 (4):3647–3652. https://www.sciencedirect.com/science/article/pii/S0957417410009656.

Zhang, X., K. Zhang, Y. Sun, Y. Zhao, H. Zhuang, W. Ban, Y. Chen, E. Fu, S. Chen, J. Liu, and Y. Hao. 2022. Combining Spectral and Texture Features of UAS-Based Multispectral Images for Maize Leaf Area Index Estimation. *Remote Sensing* 14 (2). https://www.mdpi.com/2072-4292/14/2/331.

Zhou, W., and A. Troy. 2008. An object-oriented approach for analysing and characterizing urban landscape at the parcel level. *International Journal of Remote Sensing* 29 (11):3119–3135. https://doi.org/10.1080/01431160701469065 (last accessed 24 January 2022).

Zhu, C., and X. Yang. 1998. Study of remote sensing image texture analysis and classification using wavelet. *International Journal of Remote Sensing* 19:3197–3203.